



저작자표시-비영리-변경금지 2.0 대한민국

이용자는 아래의 조건을 따르는 경우에 한하여 자유롭게

- 이 저작물을 복제, 배포, 전송, 전시, 공연 및 방송할 수 있습니다.

다음과 같은 조건을 따라야 합니다:



저작자표시. 귀하는 원저작자를 표시하여야 합니다.



비영리. 귀하는 이 저작물을 영리 목적으로 이용할 수 없습니다.



변경금지. 귀하는 이 저작물을 개작, 변형 또는 가공할 수 없습니다.

- 귀하는, 이 저작물의 재이용이나 배포의 경우, 이 저작물에 적용된 이용허락조건을 명확하게 나타내어야 합니다.
- 저작권자로부터 별도의 허가를 받으면 이러한 조건들은 적용되지 않습니다.

저작권법에 따른 이용자의 권리는 위의 내용에 의하여 영향을 받지 않습니다.

이것은 [이용허락규약\(Legal Code\)](#)을 이해하기 쉽게 요약한 것입니다.

[Disclaimer](#)

Thesis for the Degree of Master of Engineering

# Synthesis of Plasmonic Metal-Based Hybrid Nanostructures and Their Catalytic Applications



by

Devi Permatasari Zulkifli

Department of Polymer Engineering

The Graduate School

Pukyong National University

August, 2022

# Synthesis of Plasmonic Metal-Based Hybrid Nanostructures and Their Catalytic Applications

Advisor: Prof. Mun Ho Kim

by

Devi Permatasari Zulkifli



A thesis submitted in partial fulfillment of the requirements for the degree  
of

Master of Engineering

in Department of Polymer Engineering, The Graduate School  
Pukyong National University

August, 2022

# Synthesis of Plasmonic Metal-Based Hybrid Nanostructures and Their Catalytic Applications

A dissertation

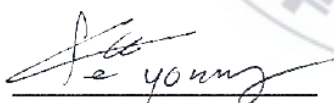
by

Devi Permatasari Zulkifli

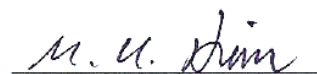
Approved by:



Prof. Dae Seok Kim



Prof. Seyoung Kee



Prof. Mun Ho Kim

August, 26<sup>th</sup>, 2022

# Contents

|  |             |
|--|-------------|
| <b>Contents</b> .....                              | <b>i</b>    |
| <b>List of Figures</b> .....                       | <b>iv</b>   |
| <b>List of Tables</b> .....                        | <b>x</b>    |
| <b>Abstract</b> .....                              | <b>xi</b>   |
| <b>요약</b> .....                                    | <b>xiii</b> |
| <b>Chapter I</b> .....                             | <b>1</b>    |
| <b>Introduction</b> .....                          | <b>1</b>    |
| I.1 Metal Nanoparticles .....                      | 1           |
| I.1.1 Synthesis of Noble Metal Nanoparticles ..... | 2           |
| I.1.2 Localized Surface Plasmon Resonance .....    | 6           |
| I.1.3 Hybrid Metal-Semiconductor .....             | 9           |
| I.1.4 Galvanic Replacement Reaction .....          | 11          |
| I.1.5 Seed Mediated Growth .....                   | 12          |
| I.2 Catalytic Applications .....                   | 13          |
| I.3 Research Scopes .....                          | 15          |

|  |           |
|--|-----------|
| <b>Chapter II.</b> .....   | <b>16</b> |
| <b>High-yield Synthesis and Hybridizations of Cu Microplates for Catalytic Applications</b> .....                    | <b>16</b> |
| II.1 Introduction .....  | 17        |
| II.2 Experimental .....  | 21        |
| II.2.1 Chemicals and Materials .....   | 21        |
| II.2.2 Synthesis of Cu microplates .....   | 21        |
| II.2.3 Synthesis of Cu@Cu <sub>2</sub> S hybrid microplates .....  | 22        |
| II.2.4 Synthesis of Cu-Au hybrid microplates .....   | 22        |
| II.2.5 Photocatalytic Activity .....   | 23        |
| II.2.6 Hydrogenation of 4-NP by NaBH <sub>4</sub> .....  | 23        |
| II.2.7 Characterization .....  | 23        |
| II.3 Results and Discussion .....  | 26        |
| II.4 Conclusions .....   | 57        |
| <b>Chapter III.</b> .....  | <b>58</b> |
| <b>Facile Synthesis and Sulfidation of PdAuAg Ternary Nanostructures and Their Photocatalytic Applications</b> ..... | <b>58</b> |
| III.1 Introduction .....   | 59        |

|  |            |
|--|------------|
| III.2 Experimental .....                         | 62         |
| III.2.1 Chemicals and Materials .....            | 62         |
| III.2.2 Synthesis of Pd Nanoplates .....         | 62         |
| III.2.3 Synthesis of PdAuAg Nanostructures ..... | 63         |
| III.2.4 Sulfidation Reaction .....               | 63         |
| III.2.5 Photocatalytic Activity .....            | 64         |
| III.2.6 Characterization .....                   | 64         |
| III.3 Result and Discussion .....                | 67         |
| III.4 Conclusions .....                          | 94         |
| <b>References .....</b>                          | <b>95</b>  |
| <b>Acknowledgment .....</b>                      | <b>118</b> |

## List of Figures

|   |    |
|---|----|
| Figure I. 1 General pathways to synthesize metal nanoparticle with different structures by the bottom-up approach [6].....  | 3  |
| Figure I. 2 Schematic diagram illustrating the localized surface plasmon on a nanoparticle surface [14] .....   | 8  |
| Figure I. 3 Schematic of Schottky junction in hybrid metal-semiconductor [27] ...   | 10 |
| Figure I. 4 Reduction of 4-nitrophenol (4-NP) to 4-aminophenol (4-AP) by NaBH <sub>4</sub> [32] .....   | 15 |
| Figure II. 1 Schematic of the overall hybridization procedures, from the synthesis of Cu microplates to the formation of Cu@Cu <sub>2</sub> S or Cu–Au hybrid microplates.....  | 25 |
| Figure II. 2 SEM images of Cu nanocrystals synthesized (a) in the absence and (b) in the presence of 1.6 μM KI. (c) XRD pattern and (d) UV–Vis–NIR spectrum of the Cu microplates shown in (b). The inset of (d) shows a photograph of an aqueous colloidal dispersion of the Cu microplates..... | 28 |
| Figure II. 3 XRD pattern of the Cu nanocrystals shown in Figure II.2(a).....  | 29 |
| Figure II. 4 AFM image and corresponding height profile of the Cu microplate shown in Figure II.2(b). The thickness of the Cu microplate was measured to be approximately 133 nm.....   | 31 |

|   |    |
|---|----|
| Figure II. 5 SEM images of Cu nanocrystals grown in the presence of KI at different concentrations: (a) 0.8 $\mu\text{M}$ , (b) 1.6 $\mu\text{M}$ , and (c) 2.4 $\mu\text{M}$ .....   | 32 |
| Figure II. 6 (a) SEM and (b) TEM images of Cu microplates grown in the presence of acetonitrile. The final concentration of KI was 1.6 $\mu\text{M}$ , and the acetonitrile-to-water ratio in the reaction medium was adjusted to $\sim 0.07$ . (c) XRD pattern and (d) UV–Vis–NIR spectrum of the Cu microplates. Inset of (d) shows a photograph of the Cu microplate aqueous colloidal dispersion grown in the presence of acetonitrile..... | 34 |
| Figure II. 7 AFM image and corresponding height profile of the Cu microplate shown in Figure II.6(a). The thickness of the Cu microplate was measured to be approximately 92 nm.....  | 35 |
| Figure II. 8 SEM images of Cu nanocrystals formed in the presence of acetonitrile. The acetonitrile-to-DI water volume ratios were (a) 0.4, (b) 0.7, and (c) 1.4, respectively.....   | 36 |
| Figure II. 9 (a) TEM image of Cu microplates grown in the presence of acetonitrile and (b) the corresponding selected-area electron diffraction pattern.....  | 38 |
| Figure II. 10 AFM image and corresponding height profile of the Cu@Cu <sub>2</sub> S hybrid microplates shown in Figure II.11. The thickness value of the hybrid microplate was measured to be approximately 131 nm.....  | 40 |
| Figure II. 11 (a) SEM and (b) TEM images, (c) XRD pattern, and (d) UV–Vis–NIR spectrum of Cu@Cu <sub>2</sub> S hybrid microplates obtained by the reaction between  |    |

|   |    |
|---|----|
| Cu microplates and Na <sub>2</sub> S. (e) STEM-EDS elemental mapping images of the Cu@Cu <sub>2</sub> S hybrid microplates.....   | 45 |
| Figure II. 12 (a) UV–Vis–NIR absorption spectra showing the photodegradation behavior of MB in the presence of Cu@Cu <sub>2</sub> S hybrid microplates under solar irradiation for 120 min. (b) Time-dependent behavior of the MB degradation and (c) photodegradation kinetics of the as-prepared Cu@Cu <sub>2</sub> S hybrid microplates. (d) Recyclability of the Cu@Cu <sub>2</sub> S hybrid microplates as photocatalysts.....                                   | 46 |
| Figure II. 13 UV–Vis–NIR absorption spectra showing the photodegradation behavior of MB in the presence of Cu microplates under sunlight irradiation for 120 min.....   | 47 |
| Figure II. 14 (a)–(b) SEM images and (c) UV–Vis–NIR spectrum of Cu–Au hybrid microplates obtained after the galvanic replacement reaction between HAuCl <sub>4</sub> and Cu microplates. (d) STEM-EDS elemental mapping images of Cu–Au hybrid microplates.....   | 49 |
| Figure II. 15 (a) UV–Vis–NIR absorption spectra of aqueous solutions of 4-NP and 4-NP mixed with NaBH <sub>4</sub> . (b) UV–Vis absorption spectra recorded at 50 s intervals and (c) plots of ln(A <sub>t</sub> /A <sub>0</sub> ) as a function of reaction time t for the catalytic hydrogenation of 4-NP and NaBH <sub>4</sub> in the presence of Cu–Au hybrid microplates. (d) Recyclability of the Cu–Au hybrid microplates for the catalytic hydrogenation..... | 54 |

|  |    |
|--|----|
| Figure II. 16 UV–Vis absorption spectra recorded at 10 min intervals for 60 min after Cu microplates were added to the solution containing 4-NP and NaBH <sub>4</sub> .....        | 55 |
| Figure III. 1 Schematic illustration of the growth route for the synthesis of PdAuAg-AgAuS hybrid nanostructures.....  | 66 |
| Figure III. 2 (A) TEM image, (B) High-resolution TEM image (Inset: FFT patterns), (C) UV-Vis-NIR spectrum of the Pd nanoplates. (D) TEM image of vertically lying nanoplates.....  | 69 |
| Figure III. 3 TEM images of Pd nanoplates formed at different amounts of citric acid: (A) 1 mL, (B) 0.5 mL, and (C) 0.25 mL.....   | 72 |
| Figure III. 4 X-ray diffraction pattern of Pd nanoplates and PdAuAg nanostructures.....  | 73 |
| Figure III. 5 PdAuAg nanostructures TEM images obtained at the reaction after (A) 10 s (B) 30 s and (C) 1 min. (D) UV-Vis spectra of the reaction solution at different times..... | 75 |
| Figure III. 6 TEM images of PdAuAg nanostructures derived by running the reaction with (A) PVP 10 kDa (B) PVP 29 kDa (C) PVP 55 kDa and (D) PVP 360 kDa. Scale bar = 50 nm. ....   | 76 |
| Figure III. 7 TEM images of PdAuAg nanostructures obtained at (A) room temperature and (B) 100oC. Scale bar = 100 nm .....   | 77 |

|  |    |
|--|----|
| Figure III. 8 (A) TEM and (B) HR-TEM images of PdAuAg nanostructures. (C) An enlarged image of the yellow box in (B) showed the twin boundaries were obtained. (D) STEM images and elemental mapping of such elements of PdAuAg nanostructures.....  | 80 |
| Figure III. 9 (A) SEM and (B) TEM images of Pd nanoplates after the addition of 0.01 M AgNO <sub>3</sub> .....   | 83 |
| Figure III. 10 TEM image of PdAu nanostructures (without the presence of Ag <sup>+</sup> ion).....   | 84 |
| Figure III. 11 TEM images of (A) PdAuAg nanostructures before and after the reaction with (B) 0.25 mL and (C) 0.5 mL of 100 mM Na <sub>2</sub> S solution.....   | 85 |
| Figure III. 12 (A-B) HR-TEM images, (C) XRD pattern of PdAuAg-AuAgS hybrid nanostructures acquired by the reaction between PdAuAg nanostructures and Na <sub>2</sub> S. (D) STEMEDS elemental mapping images of PdAuAg-AuAgS hybrid nanostructures.....  | 88 |
| Figure III. 13 Photocatalytic degradations monitored by (A) the absorption spectra for MB using PdAuAg-AuAgS hybrid nanostructures. (B-C) Photodegradation kinetics of different nanocatalysts; Pd, PdAuAg, and PdAuAg-AuAgS hybrid nanostructures. (D) Recyclability of the PdAuAg-AuAgS hybrid nanostructures as catalysts. .... | 91 |

Figure III. 14 XPS spectra of Ag 3d and Au 4f content for Ag and Au elements of PdAuAg nanostructures obtained before and after introducing Na<sub>2</sub>S solution. ....92

Figure III. 15 TEM images of PdAuAg-AuAgS hybrid nanostructures after three cycles used as photocatalyst at (A) low and (B) high magnification .....93



## List of Tables

**Table II. 1** Values of the activity parameter,  $\kappa$ , for various heterogeneous catalysts; the values of  $k$  were obtained by dividing the reaction rate constant by the total weight of used catalyst.....56



# Synthesis of Plasmonic Metal-Based Hybrid Nanostructures and Their Catalytic Applications

Devi Permatasari Zulkifli

Department of Polymer Chemistry, The Graduate School  
Pukyong National University

## Abstract

Noble-metal nanoparticles have created intensive research efforts in catalysis, electronics, sensors, and bioimaging. The majority of these applications rely on the confined surface plasmon resonance, which is peculiar to noble-metal nanostructures. At a given resonance wavelength of the input light, this localized surface plasmon resonance is coupled with charge density oscillation within the particles and causes strong electromagnetic field confinement around the nanoparticle. The properties of LSPR are highly sensitive and depend on the material shape, size, dielectric environment, and the local refractive index around nanoparticles. Thus, the nanoparticles for enhancement of these properties have been elaborated.

Compared with the monometallic nanostructures, hybrid nanostructures formed by two or more different nanomaterials are adapted to develop bimetallic and metal-semiconductor nanostructures. Hybrid nanostructures with a versatile approach to fabricate the ideal nanocatalysts that meet industrial applications have recently triggered much research interest. However, the fabrication of hybrid nanostructures with both facile, and fascinating morphology remains a challenge. In this thesis, high-performance catalysts are created

using aqueous-solution-based hybridization methods based on chemical conversion of noble metal nanostructures' surfaces. A rapid surface sulfidation was conducted to synthesize hybrid metal (bimetallic Cu-Au) and metal – semiconductor nanostructures (Cu@Cu<sub>2</sub>S and PdAuAg-AuAgS) by using sodium sulfide as the sulfur source. Characterization methods such as X-ray diffraction (XRD), scanning transmission electron microscopy (STEM), and energy dispersive X-ray spectroscopy (EDS), were employed to confirm that the as-synthesized nanoparticles were heterogeneous hybrid nanostructures.

The as-synthesized hybrid nanostructures (Cu-Au) and hybrid metal – chalcogenides semiconductor nanoparticles (Cu@Cu<sub>2</sub>S and PdAuAg-AuAgS) were suggested as an efficient catalyst for the 4-nitrophenol (4-NP) hydrogenation, and methylene blue (MB) decomposition, respectively. The reductive degradation of these pollutants in the presence of metal-semiconductor nanoparticles gave better performance compared to monometallic nanostructures. In order to achieve nanostructures with the incorporation of semiconductors, a comparison of the catalytic activity of both nanocatalysts was done. The catalytic performance of the nanocatalyst with semiconductors was found to be the best. This result confirmed the synergistic effects of charge migration and effective charge separation between those components.

플라즈모닉 금속 기반 하이브리드 나노구조체의 합성 및 촉매 소재로의 응용

Devi Permatasari Zulkifli

부경대학교 대학원 고분자공학과

### 요약

귀금속 나노 입자는 촉매, 전자, 센서 및 바이오이미징 분야에서 집중적인 연구가 진행되었다. 이러한 응용의 대부분은 귀금속 나노 구조의 고유한 광학적 특성, 즉 국소표면 플라즈몬 공명(LSPR)에 의존한다. LSPR은 입자 내 전하 밀도 진동과 관련되어 있으며 입사광의 특정 공명 파장에서 나노 입자 주위에 강한 전자기장 구속을 발생시킨다. LSPR의 특성은 매우 민감하며 물질의 모양, 크기, 유전체 환경 및 나노 입자 주변의 국소굴절률에 따라 달라진다. 따라서, 이러한 특성을 향상시키기 위해 나노 입자는 정교화 되어왔다.

단일 금속 나노 구조와 비교하여 두 개 이상의 다른 나노 물질로 형성된 하이브리드 나노 구조는 바이메탈 및 금속-반도체 나노 구조를 개발하는 데 적합하다. 산업적 적용이 가능한 이상적인 나노 촉매를 제조하기 위한 다양한 접근 방식을 가진

하이브리드 나노 구조는 최근 많은 연구 관심을 불러일으켰다. 그러나 손쉽고 매력적인 형태를 모두 갖춘 하이브리드 나노 구조의 제조는 여전히 도전 과제로 남아 있다. 본 연구에서는 고성능 촉매를 제조하기 위해 귀금속 나노 구조 표면의 화학적 전환에 기반한 수용액 기반 혼성화 접근법을 사용한다. 황화나트륨을 황 공급원으로 사용하여 하이브리드 금속 및 금속- 칼코제나이드 반도체 나노 구조체( $\text{Cu@Cu}_2\text{S}$  및  $\text{PdAuAg-AuAgS}$ )를 합성하기 위해 빠른 표면 황화를 수행했다. 투과 전자 현미경, 에너지 분산 X 선 분광법 및 X 선 회절과 같은 분석 기술을 사용하여 합성된 나노 입자가 이중 하이브리드 나노 구조임을 확인했다.

합성된 하이브리드 나노 구조체( $\text{Cu-Au}$ )와 하이브리드 금속- 칼코제나이드 반도체 나노 입자( $\text{Cu@Cu}_2\text{S}$  및  $\text{PdAuAg-AuAgS}$ )는 각각 4-니트로페놀(4-NP)의 수소화 및 메틸렌 블루(MB) 분해를 위한 효율적인 촉매로 제안되었다. 금속 반도체 나노 입자의 존재 하에서 이러한 오염 물질의 환원적 분해는 단일 금속 나노 구조에 비해 더 나은 성능을 제공했다. 두 나노 촉매의 촉매 활성을 비교한 결과 반도체를 결합한 나노 구조의 촉매 성능이 더 우수했다. 이를 통해 이들 성분 간의 전하 이동과 효과적인 전하 분리를 통한 시너지 효과를 확인했다.

# Chapter I.

## Introduction

### I.1 Metal Nanoparticles

In recent years, nanoparticles are gaining rapid interest and enthusiasm from researchers since nanoparticles have emerged as an exciting class of materials that are in high demand for a range of practical applications, such as catalysts, electronics, clean technologies, biology, and sensor. The preparation of nano-size particles ranging from 1 to 100 nm employing diverse synthesis strategies, and particle structure and size modification. The term ‘nanoparticle’ was coined from the Greek word ‘nano’ which means ‘small’ and when used as a prefix it indicates that  $10^{-9}$  one billionth of a meter is equal to 1 nm [1], [2].

Metal nanoparticles are well-known for their localized surface plasmon resonance (LSPR) characteristics, which possess unique optoelectrical properties. Nanoparticles of the noble metals i.e., Ag, Au, and Cu have a broad absorption band in the visible zone of the electromagnetic solar spectrum. In addition, LSPR sensitivity is highly dependent on the shape of nanoparticles. Other metals such as Fe, Ni, and Co were characterized as magnetism metals which have an extra useful feature of magnetic properties. They can be manipulated using magnetic fields, causing energy dissipation, and contributing to imaging contrast in the presence of

magnetic fields. Metal nanoparticle-based catalysts are structured with catalytically efficient metals such as Pd, Pt, Ru, and Ni. Metals in this category can catalyze various chemical reactions, such as coupling, and hydrogenation reactions [3], [4].

### **I.1.1 Synthesis of Noble Metal Nanoparticles**

There are two basic classes to synthesizing nanoparticles: the top-down approach and the bottom-up approach. The bottom-up approach involves the creation of nanoparticles from atoms, whereas the top-down approach involves the production of nanoparticles from macro-sized materials such as bulk metals for the initial structures. These approaches are further divided into various subclasses based on the reaction condition, operation, and adopted protocols [5], [6]. The bottom-up approach is employed in reverse as nanoparticles are formed from relatively simpler substances, building blocks of the nanoparticles first formed and then assembled to produce a final product, therefore this approach is also called the building up approach. Compared with top-down approaches, bottom-up methods offer the advantages of high consistency and high controllability of patterns' size and shape. It is convenient to modify the surface properties of nanoparticles during the synthesis process.

Based on the optimization processes for nanoparticle formation, it is very much possible to control the size and shape of the nanoparticle synthesis. Figure I.1 show the general route to synthesizing metal nanoparticle with different structures by the bottom-up approach.

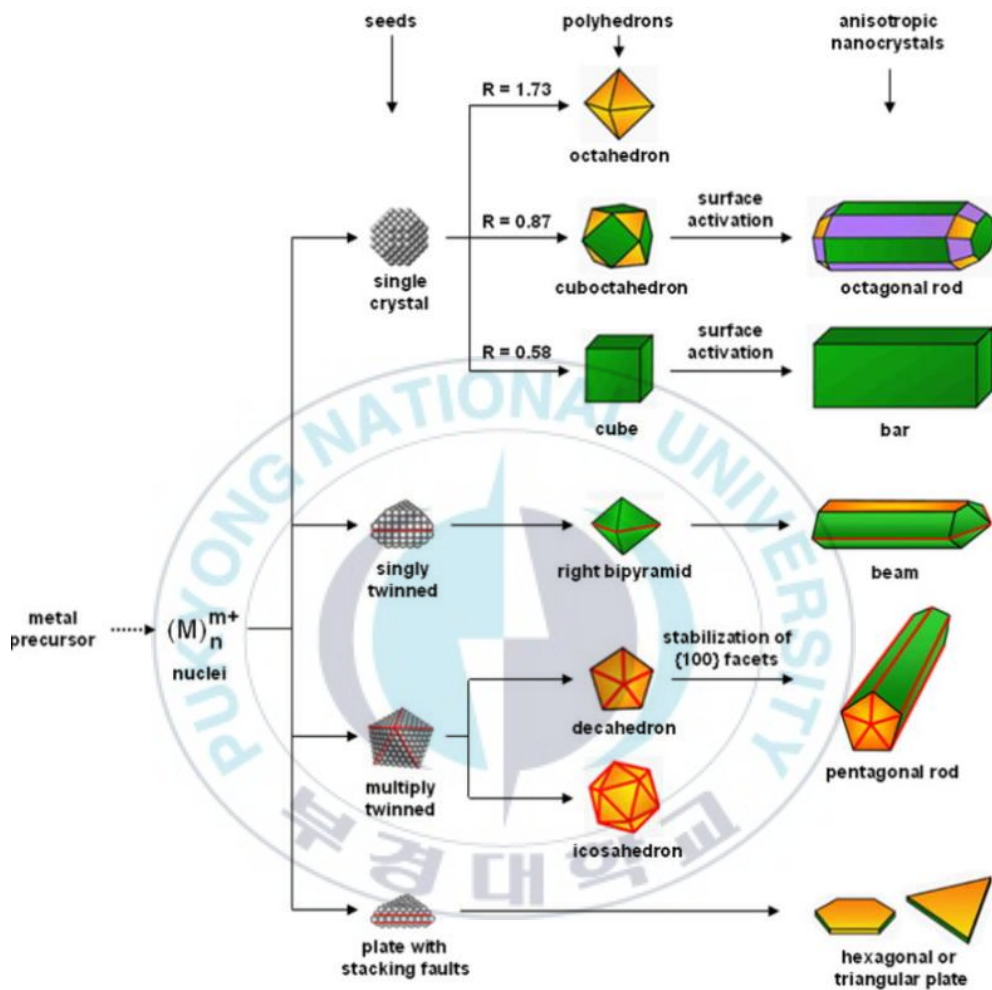
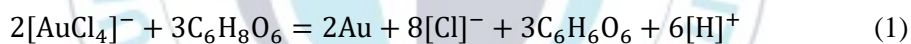


**Figure I. 1** General pathways to synthesize metal nanoparticle with different structures by the bottom-up approach [6].

In a typical synthesis of noble-metal nanoparticles, a precursor compound is reduced to generate zero-valent atoms. The concentration of metal atoms steadily increases with time as the precursor is decomposed. Once the atoms start to aggregate into small clusters i.e., nuclei. With a continuous supply of atoms via ongoing precursor decomposition, the nuclei will grow into nanocrystals. Nuclei are grown into single crystal seeds when the reduction and the generation of metal atoms are very fast. Once these nuclei have grown past a certain size, they become seeds with a single-crystal, singly twinned, or multiply twinned structure. When the reduction rate is lessened, small sizes of multiply twinned seeds tend to appear. The formation of these seeds is favored by thermodynamics and the surface of a singly twinned seed tends to be enclosed by a mix of {111} and {100} facets to lower the total interfacial free energy. If the reaction becomes extremely slow, metal atoms are hardly aggregated into seeds with thermodynamically favored structures. Therefore, a kinetically controlled method is served, and the atoms tend to form nuclei and seeds through random hexagonal close packing (RHCP), lined with the inclusion of stacking faults. The resulted nanoparticles have high surface energy and the presence of  $\frac{1}{3}\{422\}$  reflection along the {111} facet axis, and the plate-like can be formed [6].

In the synthesization of noble-metal nanoparticles, the process is relying on the chemical reduction of metal salts, electrochemical pathways, or the controlled decomposition of metastable organometallic compounds in solution. Chemical

reduction pathways consist of metal precursor salt, reducing agent, stabilizer, and solvent inorganic salts in the process. Different combinations may result in different size and structure of nanoparticles. Among those compounds, a chemical reagent containing hydroxyl groups can be employed as a reducing agent, for example, ascorbic acid. Ascorbic acid was commonly selected as a reducing agent for synthesized noble-metal nanoparticles due to its high-water solubility, biodegradability, and low toxicity compared with other chemical reducing agents such as  $\text{NaBH}_4$  [8], [9]. When ascorbic acid is used as a reductant, the redox process produces dehydroascorbic acid as the oxidized product and  $\text{H}^+$  ions. For example, ascorbic acid has been used as a reducing agent for synthesizing gold nanoparticle and the reaction equation of this system is as follow:



In This reaction process, ascorbic acid was converted to gluconic acid. By introducing an excessive ascorbic acid solution, the degree of reaction supersaturation increases and accelerates the formation of gold nanoparticles.

Furthermore, since colloidal particles prepared in the solution phase tend to agglomerate, it becomes necessary to protect them using surfactants or polymeric ligands such as polyvinyl pyrrolidone (PVP) [10]. Surfactants containing amines or thiols are essential to forming organometallic complexes in the organic solution. A secondary amine which commonly used in nanoparticle synthesis is

polyvinylpyrrolidone (PVP). PVP is considered a capping agent to kinetically control the growth rates of different crystalline facets contributing to the formation of anisotropic nanoparticles. PVP has a polyvinyl backbone with nitrogen and oxygen atoms in the polar groups. The lone pair of electrons from N and O atoms can be coordinated with metal ions by donating the electrons into sp hybrid orbitals by constructing complex compounds. The intra- and interchain interactions of PVP molecules effectively decrease the chemical potential and allow the PVP-bound metal ions to be easily reduced. The reaction mechanism for PVP to be a reducing agent is shown in the equation below:



### **I.1.2 Localized Surface Plasmon Resonance**

The absorption band results when the incident photon frequency is resonant with the collective oscillation of the conduction band electrons and is known as the localized surface plasmon resonance (LSPR). The resonance frequency of this LSPR is strongly dependent upon the size, shape, dielectric properties, and local environment of the nanoparticles. Only materials with negative real and small positive imaginary dielectric constant, are capable of supporting surface plasmons. Ag, Au, and Cu are the most common materials which exhibit plasmon resonance. When the incident electromagnetic field matches that of the oscillating electrons on the surface of the nanoparticle, a resonance condition is met. When the excited

surface electric field frequency is sufficient, the noble metal resonance leads to a dynamic utilization of visible light [11]–[13] .

Noble metals with anisotropic morphologies are expected to possess plasmon resonances coupling effect and chemical enhancement associated with the polarization state of the incident light due to the different free electron oscillations along different axes of the structures. It is the surrounding medium that determines besides size and shapes the resonance frequency of a particle. In the case of metallic particles, a decrease in size leads to a blue shift (higher frequency) while the increase of the dielectric constant of the surrounding medium leads to a redshift (lower frequency). The influence of shape can be very complex and lead to additional resonances and/or dependence of the orientation of the particle's fields are enhanced.

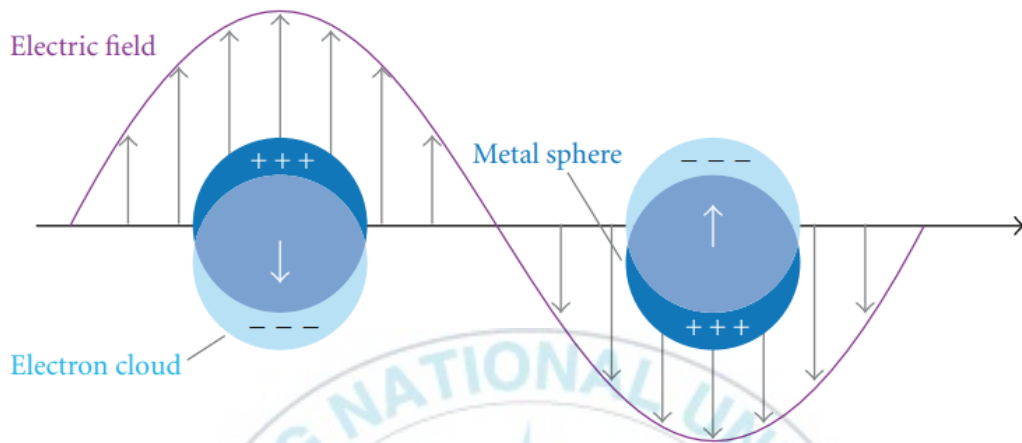


**Figure I. 2** Schematic diagram illustrating the localized surface plasmon on a nanoparticle surface [14]

### **I.1.3 Hybrid Metal-Semiconductor**

There has recently been great interest in metal-hybrid semiconductor nanoparticles since they can exhibit the physical and chemical characteristics of both the individual metal and semiconductor or display unique properties [15]. These materials possess efficient charge separation of photoexcited electrons and holes. These hybrid materials can potentially be exploited for several applications which cannot be addressed by metal-only particles. Most importantly, metal semiconductors were found to be good photocatalysis, where redox-based reactions were enhanced by the fact that photogenerated charges in the semiconductor component could be transferred to the metal tip [16], [17]. Such hybrid nanostructures combine different material components and provide a powerful strategy for modifying the properties of nanoparticles. The existence of LSPR in plasmonic metal induces plasmons and excitons in semiconductors, together with the synergistic interactions between the two components.

In addition, in the hybrid nanostructures, a Schottky barrier forms at the junction interface between the metal and semiconductor. This barrier blocks the electron transfer from the metal to the semiconductor. However, under resonant excitation of the LSPR of the metal nanocrystal, electron transfer from the metal to the semiconductor can occur during the decay of the LSPR [18]

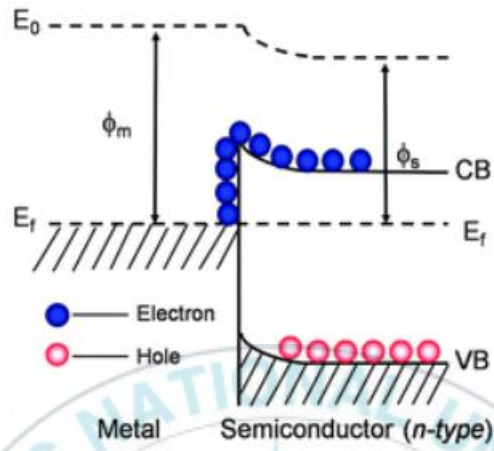


**Figure I. 3** Schematic of Schottky junction in hybrid metal-semiconductor

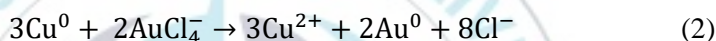
[27]

#### **I.1.4 Galvanic Replacement Reaction**

Galvanic replacement reaction is a simple and widely used approach to synthesizing alloy nanoparticle for applications in catalysis, plasmonics, and biomedical research. This method is the replacement reaction which is based on the electrical potential difference between two metals that are templates and a salt precursor in a suspension. When a metal salt solution is introduced to nanoparticles made of metal with lower reduction potential, the noble metal deposits around a nanoparticle as the nanoparticle template is concurrently removed from the inside out through gaps in the deposited layer. If the noble metal layer encapsulates the template, hollow nanostructures are formed [19], [20]. Galvanic replacement reactions are determined by thermodynamic and kinetic parameters. The thermodynamic control is necessary to minimize the total free energy of template facets, and by managing the deposition and dissolution rates, including the degree of alloying and the surface passivation, the kinetic state is controlled [21]. From Hume-Rothery rules, theoretical information for alloying is obtained, which becomes necessary for the alloying process. William Hume-Rothery suggested some rules to predict whether the two metals or one metal and one nonmetal can form a solid solution. To form a substitutional solid solution two elements must have a similar crystal structure, electronegativity, valency, and the difference between the atomic radii of solute and solvent atoms must not exceed 15%.

Alloying Cu with stable metals is proved to be an effective strategy to improve the stability since Cu is prone to oxidation. Among various metals, Au is the most widely used for alloying materials due to its good stability, tunable optical properties, and easy functionalization.

Copper nanostructures dissolved in a solution can be oxidized by HAuCl<sub>4</sub>. The standard reduction potential of the AuCl<sub>4</sub><sup>-</sup>/Au pair (1.00 V vs. standard hydrogen electrode, SHE) is much higher than that of the Cu<sup>2+</sup>/Cu pair (0.34 V vs. SHE) [22], [23]. Therefore, the replacement reaction occurred spontaneously:



Thus, Cu nanostructures can serve as sacrificial templates for the fabrication of Cu–Au bimetallic nanostructures.

### **1.1.5 Seed Mediated Growth**

Seed-mediated growth is a versatile and powerful approach to the synthesis of colloidal metal nanocrystals. During the seed-mediated growth of metal nanocrystals, the atoms tend to be deposited onto the surface of seed either at locations that have high surface energies (e.g., vertices, edges, defects, sites under a high degree of strain, edge dislocations, and high-index facets) or on regions that are not passivated by capping agents. In the simplest case of seed-mediated growth, the atoms are deposited on the entire surface of the seed to generate a conformal shell. On the other hand, the site-selected deposition was attributed to a process

that involves the galvanic replacement of a sacrificial layer underpotentially deposited at electron-rich regions such as edges and corners. It is worth emphasizing that the synthesis should be carried out in a “kinetically controlled mode” to achieve site-selected growth. Under this condition, the atoms deposited can be either partially or completely inhibited from rearranging to a configuration with lower free energy (through surface diffusion). In either case, it will result in growth on selected sites only, rather than on the entire surface of a seed [24]–[26].

## **I.2 Catalytic Applications**

Both the metal and the semiconductor components generate charge carriers and the charge migrates. A semiconductor absorbs at its band edge ( $h\nu \geq E_g$ ) and leads to an electron excitation from the valence band (VB) to the conduction band (CB), thus a hole is formed in the VB. Metal has a plasma frequency, where it absorbs light and if the solar intensity is enough at the relevant wavelength, a metal excites free electrons. Electrons from the metal and the semiconductor can participate in electron transfer. The charge and energy are transferred to the surface of the nanoparticles and meet with the molecules which will undergo a catalytic reaction [27]–[29]. Semiconductor nanoparticles possess wide bandgaps and therefore showed significant alteration in their properties with bandgap tuning. Therefore, they are very important materials in photocatalytic applications.

Aminophenol is extensively used in various industries such as dyes, pesticides, surfactants, and medicine. It is generally known that nitrophenols are very useful starting materials for producing aminophenol. The reduction of *para*-nitrophenol using sodium borohydride has become a common model reaction for the evaluation of the catalytic activity of nanomaterials in an aqueous solution, because both the *para*-nitrophenol and *para*-aminophenol have significant UV-Vis absorption peaks when in basic solution. The reduction rate of 4-NP took a long time without addition of any catalyst due to the repulsive force between negatively charged 4-NP and  $\text{BH}^{-4}$  ions. Gold and silver act as a superior catalyst, which has exposed outstanding catalytic activity in oxygen reduction and hydrogenation. This reaction development must be suitable for progressing the relaying electron transfer from donor  $\text{BH}^{-4}$  ions to the nitro group of acceptor 4-NP [30], [31].

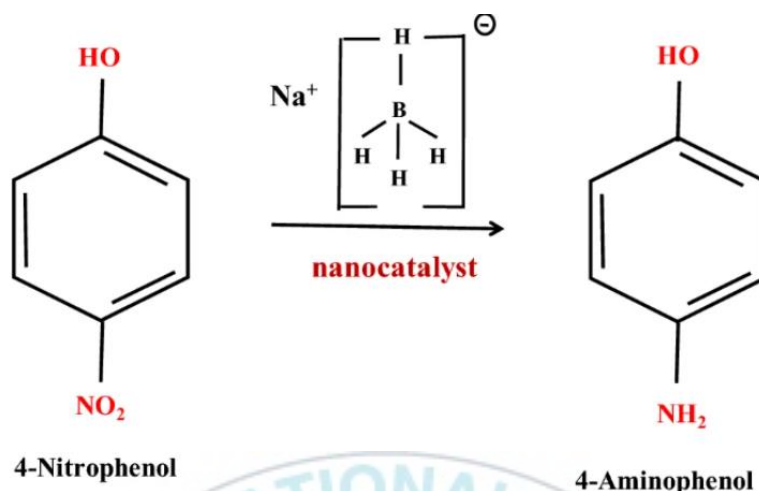


**Figure I. 4** Reduction of 4-nitrophenol (4-NP) to 4-aminophenol (4-AP) by NaBH<sub>4</sub> [32]

### I.3 Research Scopes

The object of this thesis is to develop a facile synthetic and hybridization method for generating bimetallic nanostructures and metal-semiconductor hybrid nanostructures with unique architectures and high stability. These hybrid nanostructures with outstanding synergistic properties from the two components were utilized for catalysis for hydrogenation reaction and dye degradation.

The objectives were conducted in the following way:

Chapter I. Introduction

Chapter II. High-yield Synthesis and Hybridizations of Cu Microplates for Catalytic Applications.

Chapter III. Facile Synthesis and Sulfidation of PdAuAg Ternary Nanostructures and Their Photocatalytic Applications.

## **Chapter II.**

# **High-yield Synthesis and Hybridizations of Cu Microplates for Catalytic Applications**



Reproduced with permission from

[*CrystEngComm*, 2022]

Copyright © 2022 The Royal Society of Chemistry

## II.1 Introduction

In plasmon-enhanced applications, Ag and Au nanoparticles are the most widely used metals because of their high stability and tunable strong localized surface plasmon resonance (LSPR) extinction in the ultraviolet (UV) to near-infrared (NIR) region [4], [33]–[37]. As a result of the cumulative efforts of numerous research groups, Au and Ag nanostructures with controlled size and shape have been successfully synthesized via wet chemical methods [38]–[44]. Although Ag and Au nanocrystals have shown excellent catalytic performance in the field of plasmon-enhanced catalysis, these nanocrystals have not been practically used in the chemical industry and environmental protection fields because of the high cost of Au and Ag metals [45]. Among nonprecious metals, Cu nanocrystals are an attractive alternative to noble metals in plasmon-enhanced catalysts [46]–[48]. Cu has electrical and thermal conductivities equivalent to those of Ag and Au, and Cu nanocrystals exhibit LSPR properties at wavelengths ranging from the UV to the NIR region [49]–[51]. Meanwhile, Cu is 22,000 times more abundant than Au and 1000 times more abundant than Ag [52]. However, Cu is vulnerable to attack by species such as  $O_2$  and  $H_2O$  in the ambient atmosphere, which results in a steep performance decline due to rapid oxidation. One approach to overcoming this drawback of Cu nanocrystals is to prepare hybrid nanostructures by encapsulating Cu with an inert shell [22], [53], [54].

Hybrid nanostructures formed by two or more different nanomaterials with controlled shape, size, composition, and spatial orientation have attracted considerable attention because of their superior chemical, physical, and synergistic properties compared with those of the corresponding individual components [28], [55]–[57]. Metal–semiconductor or bimetallic hybrid nanostructures have been prepared via the selective surface growth of one of the components on the other [28], [55]–[60]. However, metal–semiconductor or bimetallic hybrid nanostructures have been more efficiently synthesized by the selective chemical conversion of only a portion of the preformed metal nanostructures or by their replacement with other metal atoms [16], [20], [58], [61]–[65]. Most of these reactions proceed on the surface of the preformed metal nanostructures, and the converted or replaced materials coat the metal nanostructures' surface. Successfully adapting these strategies to Cu nanocrystals would enable the synthesis of Cu-based hybrid nanostructures with excellent stability and with outstanding synergistic properties that arise between the two components.

Compared with their bulk counterparts, two-dimensional (2D) metal nanostructures with large lateral dimensions and thin thickness have attracted widespread interest because of their anisotropic structure and fascinating properties [66]–[68]. The special geometric features of the 2D nanostructure impart high specific surface areas and high ratios of exposed surface atoms, making them promising candidates as advanced catalysts with excellent properties [69]. In

addition, because they can be easily separated from the reaction mixture by simple centrifugation after the catalytic reaction as a consequence of their relatively large size, which ranges from several to tens of micrometers, they can be used as a high-performance catalyst without support [70]. However, because 2D nanostructures are not thermodynamically favored structures as a consequence of their high surface energy and because Cu nanoplates have a higher stacking fault energy than Ag and Au nanoplates, few examples of the synthesis of high-quality 2D Cu nanostructures have been reported [10], [24], [71]–[73]. Recently, a method of synthesizing Cu microplates by adding a small amount of I<sup>-</sup> ions during the synthesis of Cu nanowires have been reported [74], [75]; however, the reaction yield of plate-shaped particles in the product is still low.

In the present study, we develop easy-to-use and rapid synthetic methods to synthesize Cu microplate-based hybrid heterostructures that exhibit unique nanoarchitectures and high stability and can be used as catalysts. A schematic of the overall hybridization procedure, from the synthesis of Cu microplates to the formation of Cu@Cu<sub>2</sub>S or Cu–Au hybrid microplates, is shown in Figure II.1. Cu microplates with large lateral dimensions and thin thickness were produced in high yield using a coordination-based protocol; here, a ligand capable of forming good coordination complexes with Cu cations (Cu(II)) played a major role. Because Cu microplates are inevitably vulnerable to oxidation because of their structural features of a high specific surface area and a high ratio of exposed surface atoms,

we attempted to synthesize Cu microplate-based hybrid nanomaterials for catalytic applications. First, Cu@Cu<sub>2</sub>S metal–semiconductor hybrid microplates were successfully prepared within 10 min via a sulfidation reaction using aqueous sodium sulfide (Na<sub>2</sub>S) under ambient conditions. To examine the photocatalytic activity and chemical stability of the Cu@Cu<sub>2</sub>S hybrid microplates, we investigated their ability to decompose methylene blue (MB) under solar irradiation. In contrast to the pure Cu microplates, which showed little photocatalytic activity, the Cu@Cu<sub>2</sub>S hybrid microplates showed excellent photocatalytic activity and sufficient chemical stability to be reused multiple times.

Finally, Cu–Au bimetallic hybrid microplates with nanocavities and a rough surface were prepared using the Cu microplates as templates for a galvanic replacement reaction with HAuCl<sub>4</sub>. When the as-prepared Cu–Au bimetallic hybrid microplates were used as catalysts for the hydrogenation of 4-nitrophenol (4-NP) to 4-aminophenol (4-AP) by NaBH<sub>4</sub>, they exhibited very high catalytic activity and showed excellent recyclability, unlike pure Cu microplates, confirming the high chemical stability of the bimetallic hybrid microplates.

## II.2 Experimental

### II.2.1 Chemicals and Materials

All reagents were of analytical grade and were used as received without further purification. Copper(II) chloride dihydrate ( $\text{CuCl}_2 \cdot 2\text{H}_2\text{O}$ ), hexadecylamine (HDA), L-ascorbic acid (AA), gold(III) chloride trihydrate ( $\text{HAuCl}_4 \cdot 3\text{H}_2\text{O}$ ), acetonitrile, polyvinylpyrrolidone (PVP;  $M_w \approx 10$  or  $55$  kDa), 4-NP, and  $\text{NaBH}_4$  were purchased from Sigma-Aldrich (USA). Sodium sulfide nonahydrate ( $\text{Na}_2\text{S} \cdot 9\text{H}_2\text{O}$ ) was purchased from Acros Organics (USA). Potassium iodide (KI) was purchased from Katayama Chemical (Japan). MB was obtained from Junsei Chemical (Japan). Chemicals were used without further purification, and deionized (DI) water was used for all reactions.

### II.2.2 Synthesis of Cu microplates

To synthesize Cu microplates (MPs), 42 mg of  $\text{CuCl}_2 \cdot 2\text{H}_2\text{O}$  was added to DI water (15 mL) under magnetic stirring. Subsequently, 0.179 g HDA, 25  $\mu\text{L}$  KI (1 M), and 1 mL of acetonitrile were introduced into the solution. The solution was then briefly vortexed ( $<10$  s) to remove agglomerates. After the solution was stirred at 9000 rpm overnight, 0.132 g AA was added to the solution and the resultant mixture was stirred until it had completely changed from blue to white. The solution was transferred to an oil bath and heated with stirring at  $85^\circ\text{C}$  for 7 h. The obtained product was centrifuged at 5000 rpm for 30 min and washed repeatedly

with an aqueous AA solution. The Cu MPs were dispersed in an aqueous AA solution with a final MP concentration of 0.8 mg/mL.

### **II.2.3 Synthesis of Cu@Cu<sub>2</sub>S hybrid microplates**

Five hundred microliters of as-synthesized Cu microplates (23.5 mM) were added to a glass vial, along with 5 mL PVP aqueous solution ( $M_w \approx 55$  kDa) with a concentration of 0.1 g/mL. Subsequently, a Na<sub>2</sub>S·9H<sub>2</sub>O solution (1 mL, 20 mM) was introduced, and the solution rapidly changed to dark brown. After 5 min of reaction, the product was centrifuged at 12,500 rpm for 8 min and washed three times with DI water to obtain Cu@Cu<sub>2</sub>S hybrid microplates.

### **II.2.4 Synthesis of Cu-Au hybrid microplates**

A 20 mL scintillation vial was filled with 2 mL of the Cu microplates (94.0 mM). AA (5.5 mL, 1 M) and 2 mL PVP ( $M_w \approx 10$  kDa, 5 wt % in DI water) were added to the vial, and the reaction mixture was stirred rapidly at room temperature for 3 min. To produce Cu-Au microplates, an aqueous solution of HAuCl<sub>4</sub> (0.5 mL, 0.025 M) was added to the vial at a rate of 10 mL/h using a syringe pump. The solution was aged for an additional 3 min at room temperature until the color of the solution had stabilized. The solution was then centrifuged at 12,500 rpm for 8 min and washed three times with DI water.

### **II.2.5 Photocatalytic Activity**

The photocatalytic activities of the Cu@Cu<sub>2</sub>S materials for the degradation of MB were evaluated under simulated solar irradiation using a Xe lamp, and the solar irradiance was adjusted to 100 mW/cm<sup>2</sup>. All experiments were carried out at room temperature. Typically, 2 mg of a Cu@Cu<sub>2</sub>S hybrid microstructure sample was dispersed in 10 mL of MB aqueous solution (concentration: 5 mg/L) and magnetically stirred in the dark for 30 min to ensure adsorption equilibrium between the MB solution and the photocatalyst. The absorbance of the aqueous solution at the maximum absorption wavelength of 664 nm was measured using UV–Vis spectroscopy to investigate the photocatalytic performance.

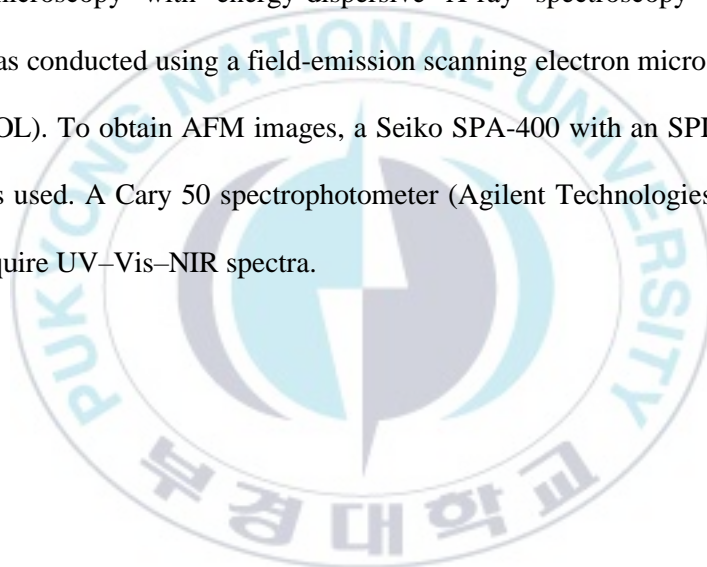
### **II.2.6 Hydrogenation of 4-NP by NaBH<sub>4</sub>**

Hydrogenation reactions were carried out at room temperature using a 4.5 mL quartz cuvette with a length of 1 cm. An aqueous solution of 4-NP (50 μL, 1 mM) and an aqueous solution of NaBH<sub>4</sub> (200 μL, 100 mM) were sequentially added to the cuvette containing 1.3 mL of DI water. Cu–Au microplates (0.04 mg) were subsequently added to the reactor, and the UV–vis absorption spectrum was recorded every 1 min.

### **II.2.7 Characterization**

Transmission electron microscopy (TEM; Hitachi H7500) at an acceleration voltage of 80 kV was used to obtain TEM images of nanostructures. Scanning

electron microscopy (SEM) images were acquired using a field-emission scanning electron microscope (TESCAN MIRA 3 LMH in-beam detector) operated at 5 kV. X-ray diffraction (XRD) patterns were obtained using a powder X-ray diffractometer (X'Pert3, PANalytical). Field-emission transmission electron microscopy (JFE-TEM, EM-2100F, Jeol), elemental mapping analysis, and high-resolution transmission electron microscopy (HR-TEM) were conducted. Scanning electron microscopy with energy-dispersive X-ray spectroscopy (SEM-EDS) analysis was conducted using a field-emission scanning electron microscope (JSM-6700F, JEOL). To obtain AFM images, a Seiko SPA-400 with an SPI-3800 probe station was used. A Cary 50 spectrophotometer (Agilent Technologies, USA) was used to acquire UV–Vis–NIR spectra.



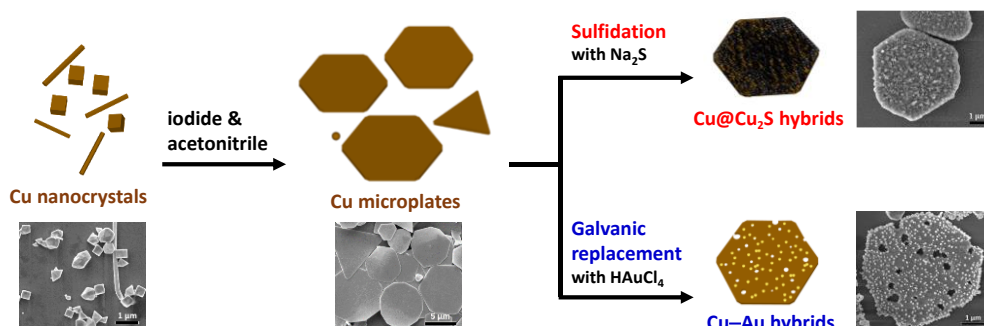
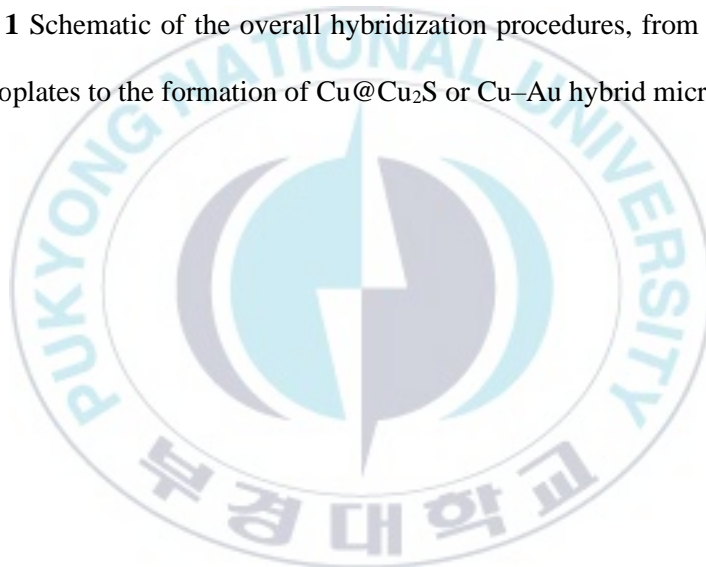


**Figure II. 1** Schematic of the overall hybridization procedures, from the synthesis of Cu microplates to the formation of  $\text{Cu}@\text{Cu}_2\text{S}$  or  $\text{Cu}-\text{Au}$  hybrid microplates



## II.3 Results and Discussion

Cu microplates were prepared by modifying the previously described water-based protocol where PVP and AA act as a colloidal stabilizer and a reducing agent, respectively. In the synthetic method,  $\Gamma^-$ , acting as a capping agent, played an important role in the formation of plate-like structures. As shown in Figure II.2(a), Cu nanocrystals having various shapes, including cubes, bipyramids, and nanowires, were obtained when  $\Gamma^-$  ions were not present. However, when  $\Gamma^-$  ions were added at a concentration of  $1.6 \mu\text{M}$  under identical experimental conditions, Cu microplates were obtained, although quasi-spherical particles were also obtained (Figure II.2(b)). As shown in Figure II.5, as the concentration of  $\Gamma^-$  ions was increased to  $1.6 \mu\text{M}$ , the yield of plate-shaped particles increased; however, at  $\Gamma^-$  ion concentrations greater than this value, the yield of plate-shaped particles decreased. The average size of the prepared Cu microplates was calculated to be  $4.3 \pm 0.6 \mu\text{m}$ . As evident from the atomic force microscopy (AFM) image of a microplate fixed onto a Si wafer and the height profile along the line in Figure II.4, the thickness of the microplate was  $\sim 133 \text{ nm}$ . The XRD pattern of the Cu microplates is shown in Figure II.2(c). The characteristic peaks at  $\sim 43.3^\circ$ ,  $\sim 50.5^\circ$ , and  $\sim 74.1^\circ$  are attributed to the  $\{111\}$ ,  $\{200\}$ , and  $\{220\}$  crystal planes of face-centered cubic (fcc) Cu, respectively, demonstrating that the synthesized Cu nanocrystals are highly pure and free of impurities, including oxides [76]. In the pattern, the peak of the  $\{111\}$  crystal plane is prominent, whereas the relative

intensities of the other peaks are low. In the XRD pattern of Cu nanocrystals shown in Figure II.2(a), the intensity ratio between the {111} and {200} diffraction peaks was found to be ~0.85 (Figure II.3). However, in the pattern of the Cu microplates, the intensity ratio increased to ~2.79. These observations indicate that Cu microplates are dominated by {111} planes and that the {111} planes tend to preferentially orient parallel to the surface of the supporting substrate [77]. The UV–Vis–NIR spectrum of an aqueous colloidal dispersion of Cu microplates is shown in Figure II.2(d). The characteristic LSPR band at 597 nm was intense and narrow, confirming the high purity of the Cu nanocrystals [78]. The inset of Figure II.2(d) shows the synthesized Cu microplate aqueous solution, which is dark-brown, typical of Cu nanocrystals.

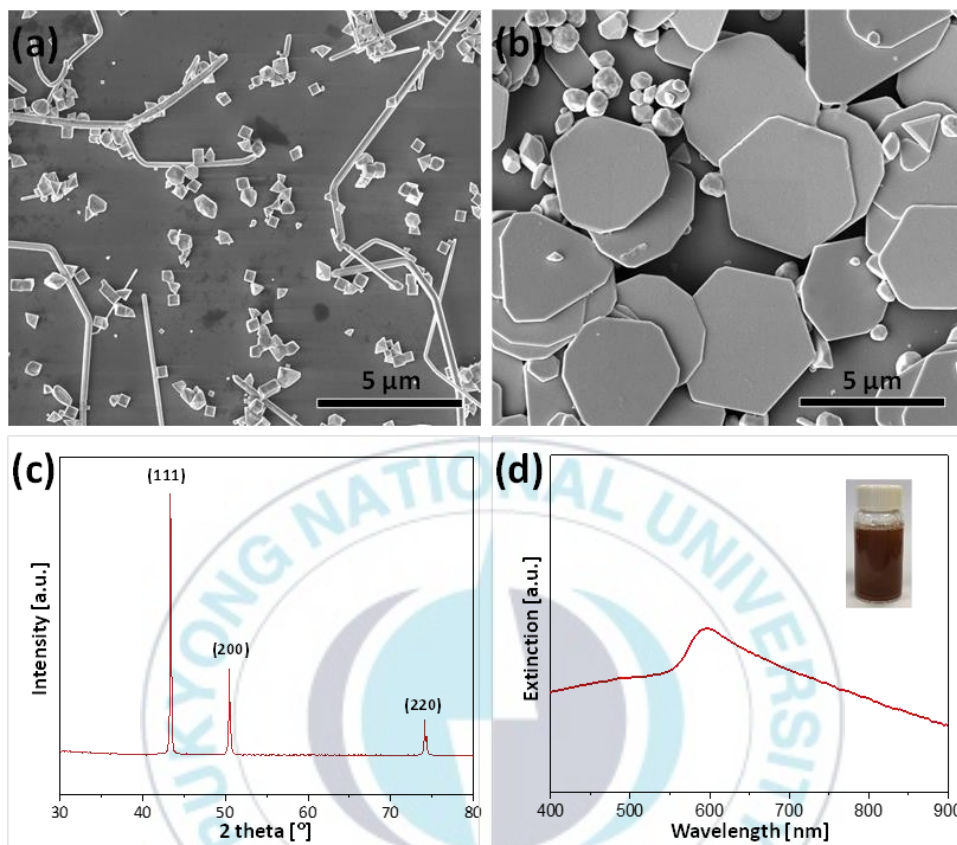


**Figure II. 2** SEM images of Cu nanocrystals synthesized (a) in the absence and (b) in the presence of 1.6  $\mu\text{M}$  KI. (c) XRD pattern and (d) UV-Vis-NIR spectrum of the Cu microplates shown in (b). The inset of (d) shows a photograph of an aqueous colloidal dispersion of the Cu microplates.

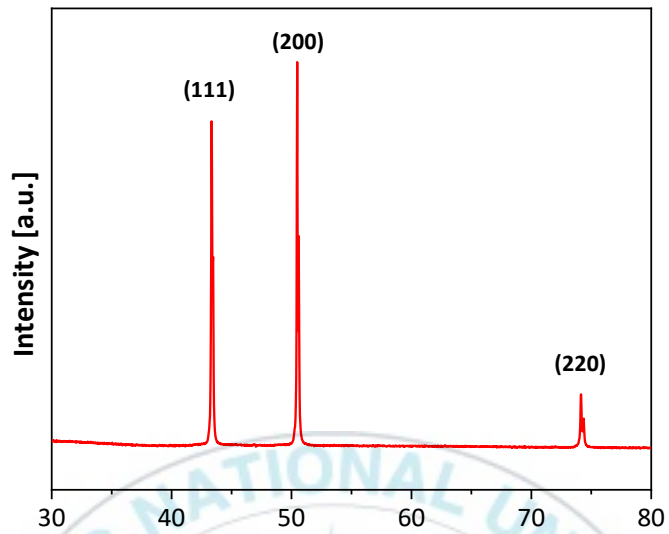
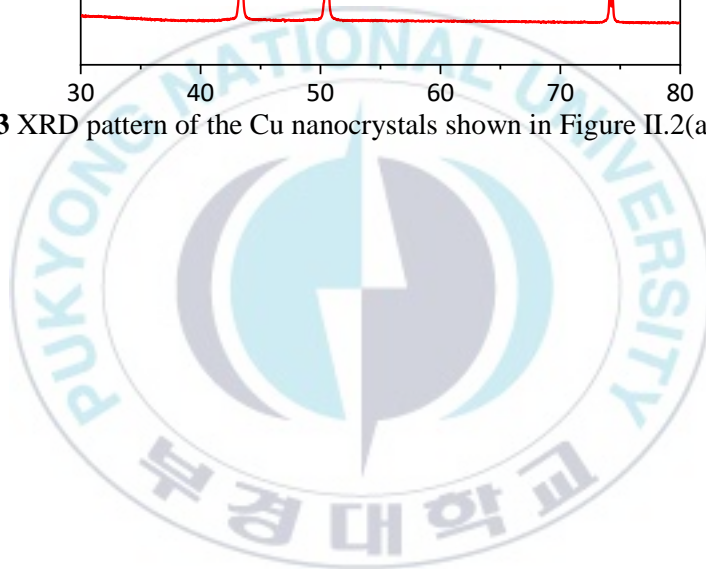


**Figure II. 3** XRD pattern of the Cu nanocrystals shown in Figure II.2(a).



In the present study, a small amount of acetonitrile was added to the reaction medium (water) to increase the yield of microplates in the final products. Acetonitrile is known to act as a ligand to form a complex with metal ions [79], [80]. This coordination effect can substantially lower the reduction rate of  $\text{Cu}^{2+}$  ions and consequently reduce the equilibrium concentration of Cu atoms. As a result, the continuous formation of nucleation sites is suppressed and the number of seeds is reduced in the nucleation step [80]. In this way, by reducing only the number of seeds while maintaining a constant Cu precursor concentration, larger Cu microplates can be formed with high yield.

In the synthesis of Cu nanocrystals, the progress of the reaction can be monitored by observing the unique color change [48]. After AA was injected into the reaction mixture containing a Cu precursor ( $\text{CuCl}_2 \cdot 2\text{H}_2\text{O}$ ), HDA, and KI, the blue-colored aqueous solution became white, indicating reduction of the  $\text{Cu}^{2+}$  ions. When the reaction mixture was heated at  $85^\circ\text{C}$  for 1 h, it changed from white to bright-yellow, orange, and reddish-brown. The solution then changed to brown and dark-brown over the course of 7 h. However, when acetonitrile was added, the color change of the reaction was relatively slow and the reddish-brown color appeared after 2 h. This result indicates that the reaction was slower when acetonitrile was present. [48]

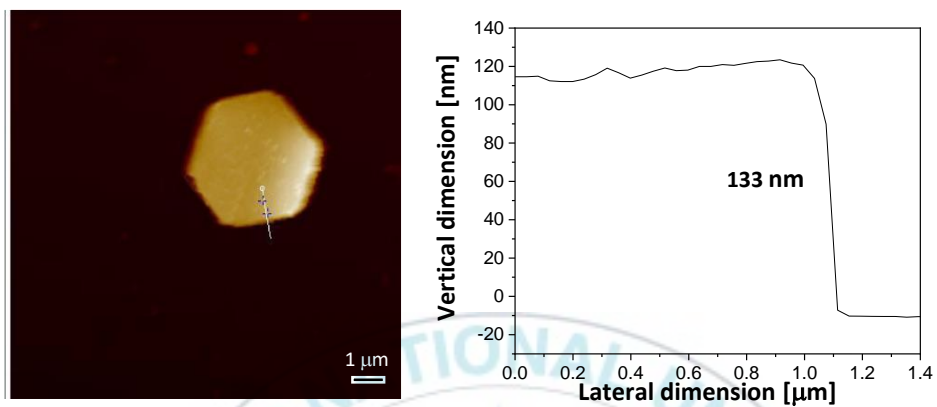


**Figure II. 4** AFM image and corresponding height profile of the Cu microplate shown in Figure II.2(b). The thickness of the Cu microplate was measured to be approximately 133 nm.

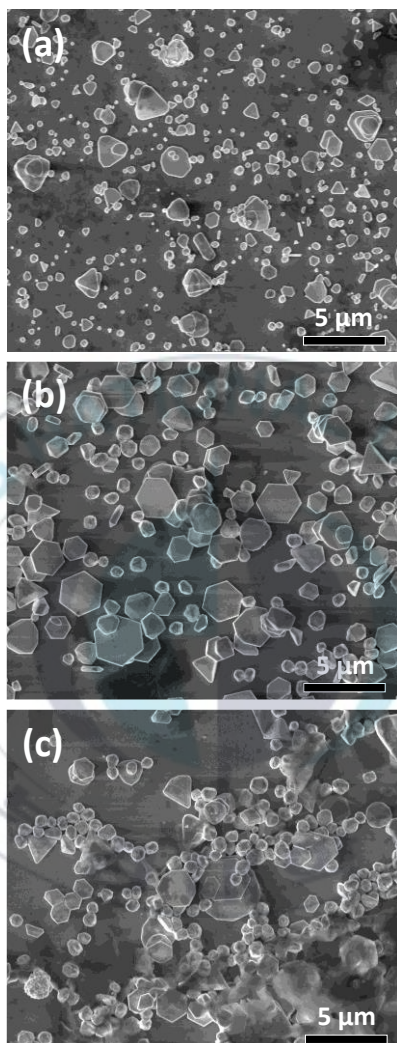


**Figure II. 5** SEM images of Cu nanocrystals grown in the presence of KI at different concentrations: (a) 0.8  $\mu\text{M}$ , (b) 1.6  $\mu\text{M}$ , and (c) 2.4  $\mu\text{M}$ .

Figure II.6 (a)-(b) shows SEM and TEM images, respectively, of the products obtained under the same conditions in the presence of acetonitrile. When acetonitrile was introduced, the yield of the plates (the percentage of plate-like structures in products) increased from 65.4% to 95.1% and the lateral dimensions of the obtained nanoplatelets also increased to  $5.8 \pm 1.3 \mu\text{m}$ . Figure II.7 shows the AFM image and corresponding height profile of a Cu microplate. The average thickness was measured to be  $\sim 92 \text{ nm}$ , indicating that the aspect ratio of the microplates was substantially increased. These results indicate that the growth path of Cu microplates was dramatically affected by acetonitrile and that lateral growth was promoted, consistent with our expectations. In this experiment, the optimal acetonitrile-to-water ratio was found to be  $\sim 0.07$ . According to our experimental results, as the acetonitrile-to-water ratio was increased to 0.07, the yield of plate-shaped particles among the total particles obtained increased (Figure II.8). However, when it was increased to greater than 0.07, the particle size of the obtained microplates was smaller, with collapse of the microplates.

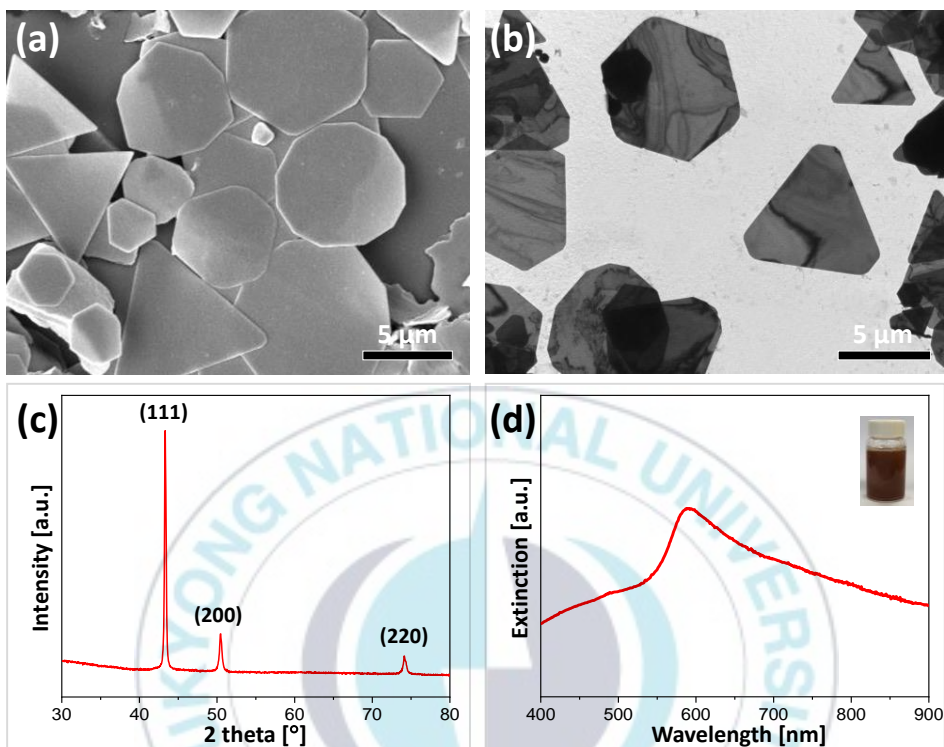


**Figure II. 6** (a) SEM and (b) TEM images of Cu microplates grown in the presence of acetonitrile. The final concentration of KI was 1.6  $\mu\text{M}$ , and the acetonitrile-to-water ratio in the reaction medium was adjusted to  $\sim 0.07$ . (c) XRD pattern and (d) UV-Vis-NIR spectrum of the Cu microplates. Inset of (d) shows a photograph of the Cu microplate aqueous colloidal dispersion grown in the presence of acetonitrile.

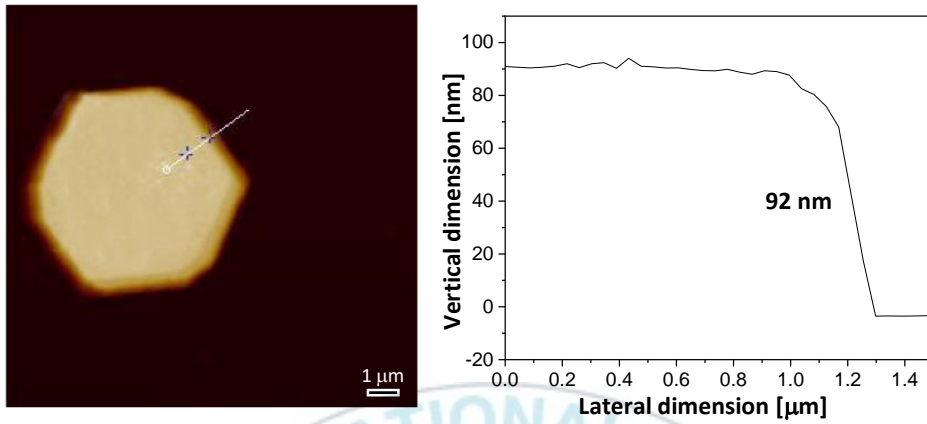


**Figure II. 7** AFM image and corresponding height profile of the Cu microplate shown in Figure II.6(a). The thickness of the Cu microplate was measured to be approximately 92 nm.

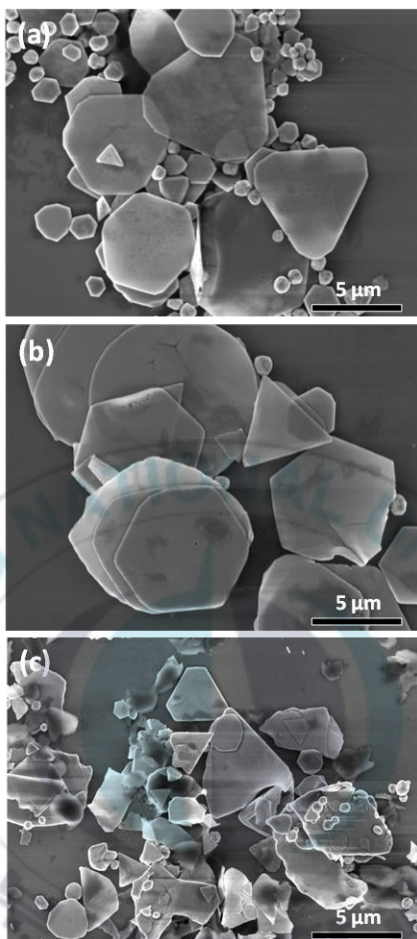


**Figure II. 8** SEM images of Cu nanocrystals formed in the presence of acetonitrile. The acetonitrile-to-DI water volume ratios were (a) 0.4, (b) 0.7, and (c) 1.4, respectively.

The XRD pattern of the Cu microplates grown in the presence acetonitrile is shown in Figure II.6(c). This pattern does not substantially differ from that shown in Figure II.2(c); however, the intensity ratio between the {111} and {200} diffraction peaks increased to  $\sim 4.41$ , which confirms that both the yield of plate-shaped particles and the lateral dimension of the synthesized microplates increased when acetonitrile was present [81]. The selected-area electron diffraction pattern of the Cu microplates was obtained to gain insight into their crystal structure (Figure II.9). The six diffraction points with six-fold rotational symmetry confirmed that the microplate has a single-crystal structure with the {111} crystal plane as the principal plane, consistent with the results of the XRD analysis [74]. The circled and the boxed spots are indexed as {220} and formally forbidden  $(1/3)\{422\}$  Bragg reflections (Figure II.9(b)), respectively, in agreement with the reported geometrical model of fcc metal nanostructures with plate-like structures[82-84]. Figure II.6(d) displays the UV-Vis-NIR spectrum of the aqueous colloidal dispersion of Cu microplates synthesized after the addition of acetonitrile. Although the position of the LSPR band hardly changed, the intensity of the peak increased, indicating that the shape uniformity of the reaction product was improved by the increase of the yield of the plate-shaped particles.

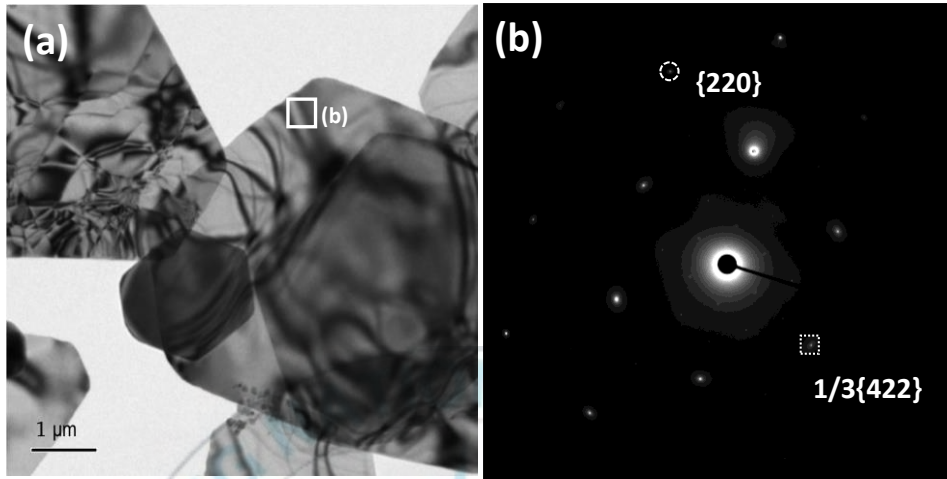


**Figure II. 9** (a) TEM image of Cu microplates grown in the presence of acetonitrile and (b) the corresponding selected-area electron diffraction pattern.

The increase in the yield and particle size of the plate-shaped particles upon the addition of acetonitrile is explained as follows. For the shape-controlled synthesis of metal nanocrystals, precisely controlling the reduction kinetics of Cu(II) ions is important. Because of the relatively large surface area and the lattice deformation energy due to defects, the total free energy of the plate-shaped particles is high [85]. Consequently, the formation of plated-shaped particles is not thermodynamically favored and can only be achieved by driving the reaction under fully kinetically controlled conditions [86]. When acetonitrile is introduced, Cu(II) ions can react with the acetonitrile to form intermediate species, which can act as a reservoir to inhibit the supersaturation of the Cu(II) ions in the solution [80]. Accordingly, the reduction reaction is substantially slowed, and the formation of nanocrystals is critically influenced by the reaction kinetics, not the reaction thermodynamics. As a result, plate-shaped particles can be efficiently formed. In addition, the slow reduction rate of Cu(II) ions will reduce the number of nuclei formed by suppressing their continuous formation. On the basis of the Gibbs–Thomson equation, a slow reduction rate favors the growth of newly formed Cu atoms onto existing seeds, whereas a fast reaction rate favors self-nucleation [24]. Thus, when acetonitrile is introduced into the reaction system, large microplates can be formed because more Cu atoms are added to the already formed plate-shaped particles.

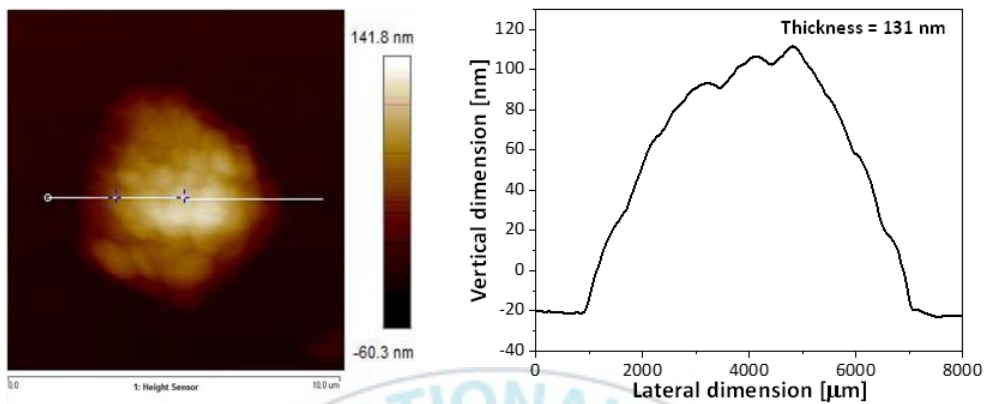


**Figure II. 10** AFM image and corresponding height profile of the Cu@Cu<sub>2</sub>S hybrid microplates shown in Figure II.11. The thickness value of the hybrid microplate was measured to be approximately 131 nm.

Nanocrystals of  $\text{Cu}_2\text{S}$ , an important p-type semiconductor, have been investigated because of their substantial advantages, which include strong absorption, high photostability, and low toxicity [87–92]. They have strong potential in a wide range of applications, including solar cells, photocatalysts, thermoelectric materials, and high-capacity anode materials for lithium secondary batteries [93-97].  $\text{Cu@Cu}_2\text{S}$  hybrid nanostructures can be effectively synthesized by exposing preformed Cu nanocrystals to sulfur compounds in various oxidation states to transform them into sulfides [89]. Although the sulfidation reaction proceeds as an aqueous solution process, it relies on toxic chemicals such as hydrogen sulfide and ammonium sulfide as a sulfur source, which are highly volatile and thus make precise control of the reaction difficult [98]. In the present study, a strategy was adopted to synthesize  $\text{Cu@Cu}_2\text{S}$  hybrid nanostructures in an aqueous solution at room temperature using sodium sulfide ( $\text{Na}_2\text{S}$ ) as a source of sulfur because  $\text{Na}_2\text{S}$  is soluble and abundant in water and is relatively less harmful than hydrogen sulfide or ammonium sulfide [98-99]. Because the sulfidation reaction would occur mainly on the surface of the Cu crystal,  $\text{Cu}_2\text{S}$  is completely coated onto the surface of the Cu nanocrystals after the reaction, eventually resulting in a core (Cu)/shell ( $\text{Cu}_2\text{S}$ ) structure.

Figure II.11(a)–11(b) shows SEM and TEM images of  $\text{Cu@Cu}_2\text{S}$  hybrid microplates obtained after a specific concentration of  $\text{Na}_2\text{S}$  aqueous solution was added and the solution was aged at room temperature for 5 min. The top and

bottom surfaces of the microplates, which were originally uniform and smooth, became very rough. The surface of the hybrid microplate is very rough, and its thickness was measured to be ~131 nm, indicating that the thickness was increased by the sulfidation reaction. The crystallographic structure of the sample shown in Figure II.11(a)–11(b) was investigated by XRD analysis; Figure II.11(c) shows the corresponding results. We confirmed that new peaks were generated after the sulfurization with Na<sub>2</sub>S; these peaks are assigned to Cu<sub>2</sub>S (JCPDS file no. 84-1770) [100]. These results demonstrated that Cu microplates were successfully converted to Cu@Cu<sub>2</sub>S hybrid microplate. UV–Vis–NIR spectroscopy was used to investigate the optical properties of the formed Cu@Cu<sub>2</sub>S hybrid microplates. The spectrum (Figure II.11(d)) shows a broadband absorption in the 300–800 nm wavelength region. Accordingly, the aqueous colloidal dispersion of the hybrids appeared dark-gray, as shown in the inset of the figure. The relative positions of Cu and S within individual hybrid microplates was determined by energy-dispersive X-ray spectroscopy (STEM-EDS) mapping analysis. As shown in Figure II.11(e), Cu and S were homogeneously distributed. Collectively, these results confirm that Cu@Cu<sub>2</sub>S hybrid microplates can be obtained within a short time via the chemical conversion of the surface of Cu microplates to Cu<sub>2</sub>S with Na<sub>2</sub>S in an aqueous solution at room temperature. In the present study, the optimal concentration of Na<sub>2</sub>S in the aqueous solution used for the sulfidation process was approximately 0.3 mM. When the Na<sub>2</sub>S concentration was less than 0.3 mM, little change was

observed in the morphologies of the microplates; when it was greater than 0.3 mM, the microplates were broken.

According to a series of recent studies, metal–semiconductor hybrid nanocrystals can be used as high-performance and efficient photocatalysts [101-102]. Compared with Cu nanocrystals, Cu@Cu<sub>2</sub>S hybrid nanocrystals can be more effective photocatalysts because of their broadband absorption properties and excellent chemical stability as a result of the incorporation of Cu<sub>2</sub>S [103]. To investigate the photocatalytic activity of hybrid microplates, we carried out photooxidative degradation of the organic dye MB under solar irradiation in the presence of the as-synthesized Cu microplates or Cu@Cu<sub>2</sub>S hybrid microplates. Figure II.12(a) shows the time-dependent MB decomposition behavior in the presence of the Cu@Cu<sub>2</sub>S hybrid microplates under solar irradiation. After 120 min of reaction, almost 85% of the MB was degraded, which is a substantial improvement compared with the results obtained with the pure Cu microplates (Figure II.13). Figure II.12(b) shows the time-dependent degradation of MB under solar irradiation in the presence of Cu microplates or Cu@Cu<sub>2</sub>S hybrid microplates. In the figure, C<sub>0</sub> represents the initial MB concentration and C<sub>t</sub> represents the MB concentration at reaction time t. The photocatalytic performance was greatly improved under identical reaction conditions after Cu was combined with Cu<sub>2</sub>S through the sulfidation reaction. For a quantitative comparison, ln(C<sub>0</sub>/C<sub>t</sub>) is plotted as a function of t in Figure II.12(c), which shows a linear relationship. These results indicate that the photocatalytic

degradation of MB follows a pseudo-first-order kinetic equation:  $\ln(C_0/C_t) = K_{app}t$ , where  $K_{app}$  is the apparent rate constant [16]. The  $K_{app}$  for Cu@Cu<sub>2</sub>S hybrid microplates was determined to be 0.0162 min<sup>-1</sup>, which is substantially greater than that of the pure Cu microplates (0.0006 min<sup>-1</sup>).

Catalyst recovery and reuse are one of the most important considerations when evaluating a catalyst's practical effectiveness [104]. Because the Cu@Cu<sub>2</sub>S hybrid microplates reached several micrometers in size, they were easily separated from the reaction solution by centrifugation after the photocatalytic reaction. The hybrid microplates were used in multiple reaction cycles to investigate their reusability as photocatalysts. The results in Figure II.12(d) confirm that the catalytic activity of the hybrid microplates was still high even after three additional cycles. A TEM image of the Cu@Cu<sub>2</sub>S hybrid microplates after three additional MB photodegradation cycles clearly shows that the structure of the hybrid microplate remained intact even after three additional cycles, demonstrating the excellent photocatalytic stability of the Cu@Cu<sub>2</sub>S hybrid nanoplates.

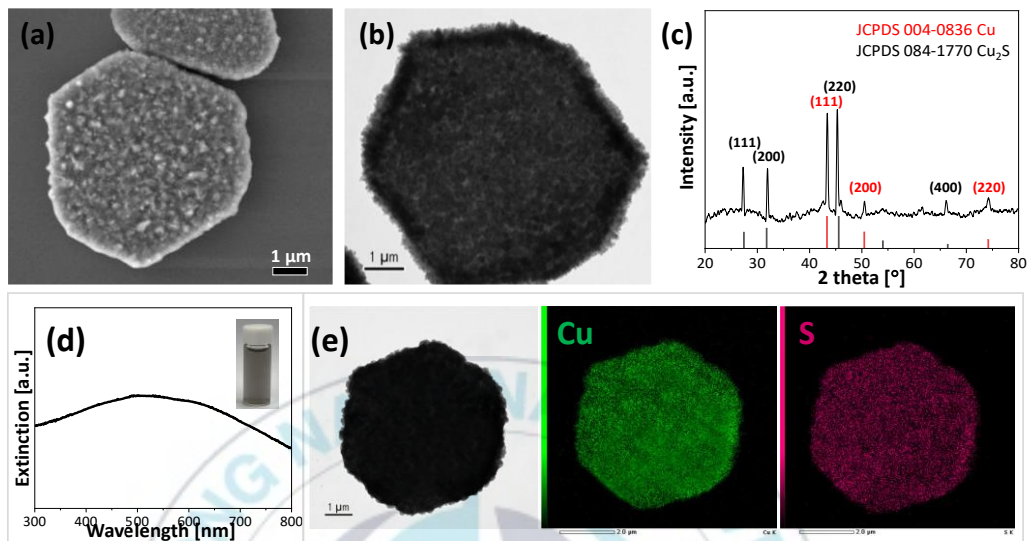


**Figure II. 11** (a) SEM and (b) TEM images, (c) XRD pattern, and (d) UV-Vis-NIR spectrum of Cu@Cu<sub>2</sub>S hybrid microplates obtained by the reaction between Cu microplates and Na<sub>2</sub>S. (e) STEM-EDS elemental mapping images of the Cu@Cu<sub>2</sub>S hybrid microplates.

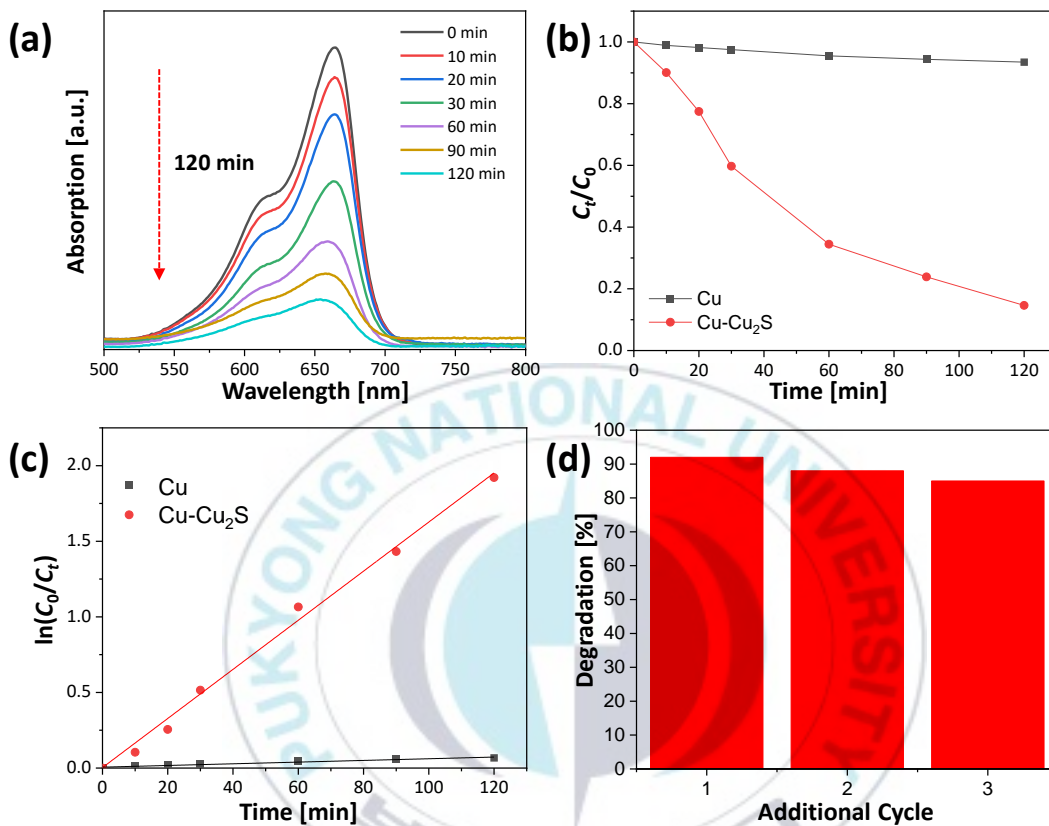


**Figure II. 12** (a) UV-Vis-NIR absorption spectra showing the photodegradation behavior of MB in the presence of Cu@Cu<sub>2</sub>S hybrid microplates under solar irradiation for 120 min. (b) Time-dependent behavior of the MB degradation and (c) photodegradation kinetics of the as-prepared Cu@Cu<sub>2</sub>S hybrid microplates. (d) Recyclability of the Cu@Cu<sub>2</sub>S hybrid microplates as photocatalysts.

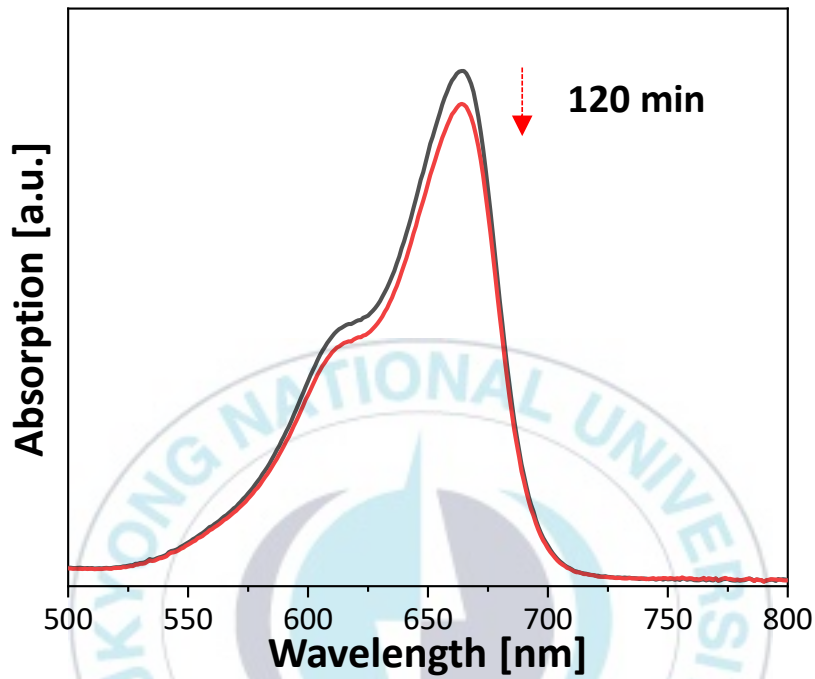


**Figure II. 13** UV-Vis-NIR absorption spectra showing the photodegradation behavior of MB in the presence of Cu microplates under sunlight irradiation for 120 min.

Galvanic replacement reactions provide a simple and versatile route for producing bimetallic nanocrystals with porous architectures. When a metal ion with a higher reduction potential contacts another metal with a lower reduction potential in an electrolyte, an electrochemical reaction occurs spontaneously and the metal with a lower reduction potential tends to be corroded [20]. Specifically, when a noble-metal salt solution is introduced into an aqueous suspension of metal nanocrystals having a lower reduction potential, the metal nanocrystals undergo spontaneous oxidation while the noble metal ions are reduced and deposit onto the surface of the nanocrystals [105]. In principle, Cu nanostructures can serve as sacrificial templates for the fabrication of Cu–Au bimetallic nanostructures [106]. The standard reduction potential of the  $\text{AuCl}_4^-/\text{Au}$  pair (1.00 V vs. standard hydrogen electrode, SHE) is much higher than that of the  $\text{Cu}^{2+}/\text{Cu}$  pair (0.34 V vs. SHE) [107]. Therefore, the replacement reaction ( $3\text{Cu}^0 + 2\text{AuCl}_4^- \rightarrow 3\text{Cu}^{2+} + 2\text{Au}^0 + 8\text{Cl}^-$ ) occurred spontaneously. Because the reaction involves the stoichiometric replacement of 3 Cu atoms with 2 Au atoms, cavities can form on the Cu nanocrystals' surface after the reaction, resulting in the formation of Cu–Au bimetallic nanostructures with porous structures [108].

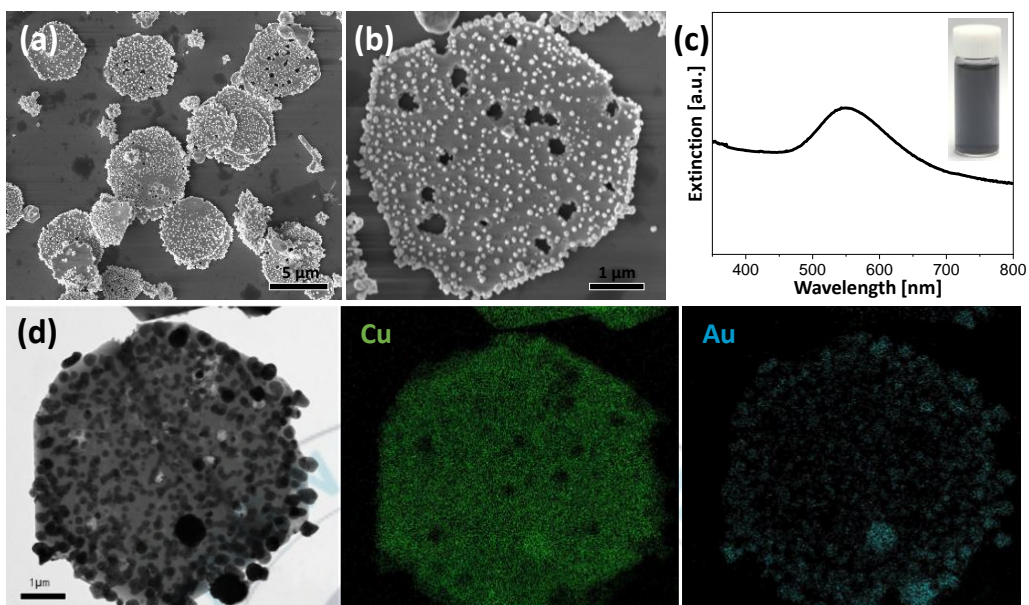


**Figure II. 14** (a)–(b) SEM images and (c) UV–Vis–NIR spectrum of Cu–Au hybrid microplates obtained after the galvanic replacement reaction between  $\text{HAuCl}_4$  and Cu microplates. (d) STEM-EDS elemental mapping images of Cu–Au hybrid microplates.

When a  $\text{HAuCl}_4$  aqueous solution was added to the aqueous dispersion of Cu microplates synthesized in the presence of acetonitrile, the aqueous dispersion changed from brown to blue-gray, indicating that the galvanic replacement reaction occurred immediately. Figure II.14(a)–14(b) shows SEM images of the resultant Cu–Au hybrid nanostructures prepared after the addition of an aqueous  $\text{HAuCl}_4$  solution. The Cu–Au hybrid nanostructures maintained their plate shape and size distribution after the galvanic reaction; however, several nanocavities were created on the surface of an individual microplate. In addition, numerous small nanocrystals were observed on the surfaces of the Cu microplates after the galvanic replacement reaction. These nanocrystals are expected to be Au nanocrystals. After  $\text{AuCl}_4^-$  ions were reduced to metallic Au on the surface of the Cu microplates, the large lattice mismatch (12.7%) between Cu (0.3615 nm) and Au (0.4079 nm) and the poor miscibility of the Cu–Au binary system at low temperatures prevented the formation of homogeneous alloy nanostructures; thus, Au nanocrystals grew epitaxially on the surface of the Cu microplates, unlike the galvanic replacement reaction between  $\text{HAuCl}_4$  and Ag nanocrystals [52]. EDX measurements of the hybrid microplates indicated a composition of 59% Cu and 30% Au. Figure II.14(c) shows that these microparticles exhibit an LSPR extinction peak at 554 nm, indicating that the peak was slightly blue-shifted after the galvanic replacement reaction. Given that the surface plasmon resonance for small Au nanoparticles appears at wavelengths near 500 nm, this change in LSPR properties occurred

because alloy structures of Cu microplates and Au nanocrystals were formed through the galvanic replacement reaction. The element mapping images of the Cu–Au hybrid microplates are displayed in Figure II.14(d), in which the green and blue dots represent the elements Cu and Au, respectively. These results reveal that the hybrid microplate consists of principally Cu and Au nanocrystals decorated on the surface of the microplate, consistent with the results of SEM and LSPR analysis.

The Cu–Au hybrid microplates have several cavities on the surface, and numerous small Au nanocrystals exist on the surface and edges of the microplates. Because of these unique porous structures and the surface roughness, the microplates can provide numerous active sites and sites suitable for catalytic reactions; thus, the microplates can be widely applied in catalysis [63]. In the present study, the reduction of 4-NP to 4-AP by  $\text{NaBH}_4$  was chosen as a probe reaction to demonstrate the catalytic performance of the Cu–Au hybrid microplates. 4-NP, which is widely used in pesticides and dye, is one of the most toxic and dangerous contaminants [84]. Accordingly, the hydrogenation of 4-NP to 4-AP using  $\text{NaBH}_4$  is potentially important because it is an environmentally friendly and effective method to remove 4-NP in an aqueous phase. The hydrogenation reaction from 4-NP to 4-AP by  $\text{NaBH}_4$  takes several days; thus, a stable and efficient catalyst is needed to drastically reduce the reaction time.

We used the prepared Cu–Au hybrid microplates as catalysts in the hydrogenation reaction of 4-NP to 4-AP by  $\text{NaBH}_4$ . First, upon the addition of  $\text{NaBH}_4$  to the 4-NP

aqueous solution, the absorption peak at 318 nm shifted to 400 nm because 4-NP was transformed to 4-nitrophenolate ion (Figure II.15(a)) [109]. The UV-Vis spectra recorded at 50 s time intervals after the Cu-Au hybrid microplates were added to the aqueous solution containing 4-NP and NaBH<sub>4</sub> are shown in Figure II.15(b). The intensity of the absorption peak at 400 nm gradually decreased with time and reached almost zero after 300 s. Simultaneously, an absorption peak at 301 nm appeared and increased in intensity with time, revealing that the hydrogenation reaction was successfully carried out. In this experiment, the reaction rate constant (k) can be calculated on the basis of the pseudo-first-order reaction formula because NaBH<sub>4</sub> was added in excess and the reaction rate therefore did not depend on the concentration of NaBH<sub>4</sub> [109]. Figure II.15(c) displays a plot of ln(A<sub>t</sub>/A<sub>0</sub>) and reaction time t, where A<sub>t</sub> and A<sub>0</sub> are the absorbance at time t and at time 0, respectively. The k value of the Cu-Au hybrid microplates used in the present study was calculated to be  $11.6 \times 10^{-1} \text{ s}^{-1}$ . On the contrary, the absorption spectra of the hydrogenation reaction performed using pure Cu microplates as catalysts changed only slightly over 60 min (Figure II.16); thus, the hydrogenation reaction progressed very slowly, indicating that the pure Cu microplates exhibited poor catalytic activity.

Because the Cu-Au hybrid microplates used in the present study have a large particle size of several micrometers, they can be easily collected from the reaction mixture and reused after the catalytic reaction is complete. The reusability of

catalysts was evaluated in experiments where the same hybrid microplates were used repeatedly. During five reuse cycles, the catalytic activity based on the conversion rate of 4-NP was found to be almost identical, showing that the catalysts exhibit excellent reusability and excellent stability (Figure II.15(d)). To quantitatively compare the catalytic activity of the Cu–Au hybrid microplates with those of other reported catalysts, we calculated the activity parameter  $\kappa$  ( $= k/m$ ), where  $m$  is the total mass of catalyst added to the reaction and  $k$  is the rate constant for the hydrogenation reaction [104]. The  $\kappa$  value in the reaction using the hybrid microplates as catalyst was calculated to be  $166 \text{ s}^{-1} \text{ g}^{-1}$ . This value is high compared with those reported for heterogeneous catalysts based on metal nanostructures used for the hydrogenation of 4-NP to 4-AP by  $\text{NaBH}_4$  (Table II.1).

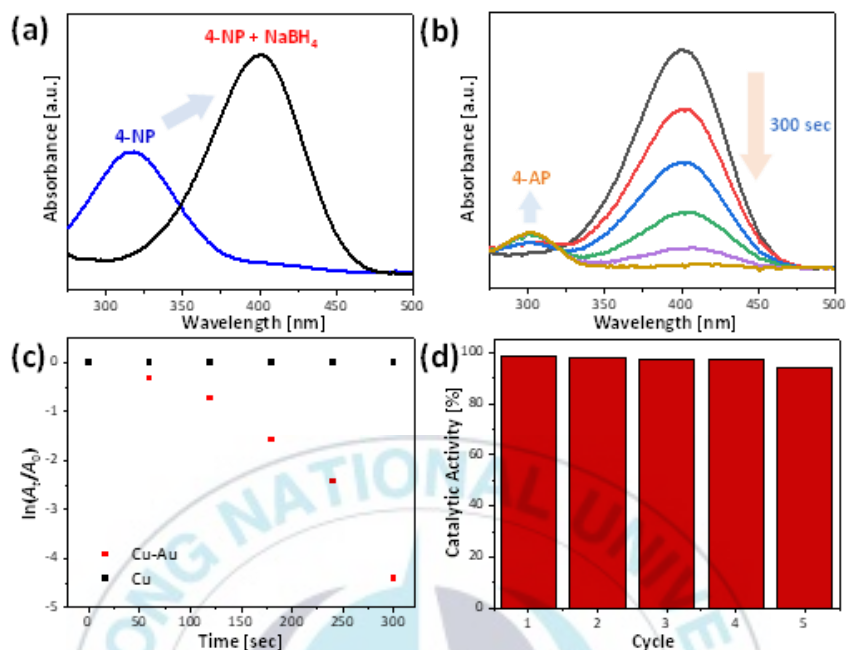


**Figure II. 22** (a) UV-Vis-NIR absorption spectra of aqueous solutions of 4-NP and 4-NP mixed with NaBH<sub>4</sub>. (b) UV-Vis absorption spectra recorded at 50 s intervals and (c) plots of  $\ln(A_t/A_0)$  as a function of reaction time  $t$  for the catalytic hydrogenation of 4-NP and NaBH<sub>4</sub> in the presence of Cu-Au hybrid microplates. (d) Recyclability of the Cu-Au hybrid microplates for the catalytic hydrogenation.

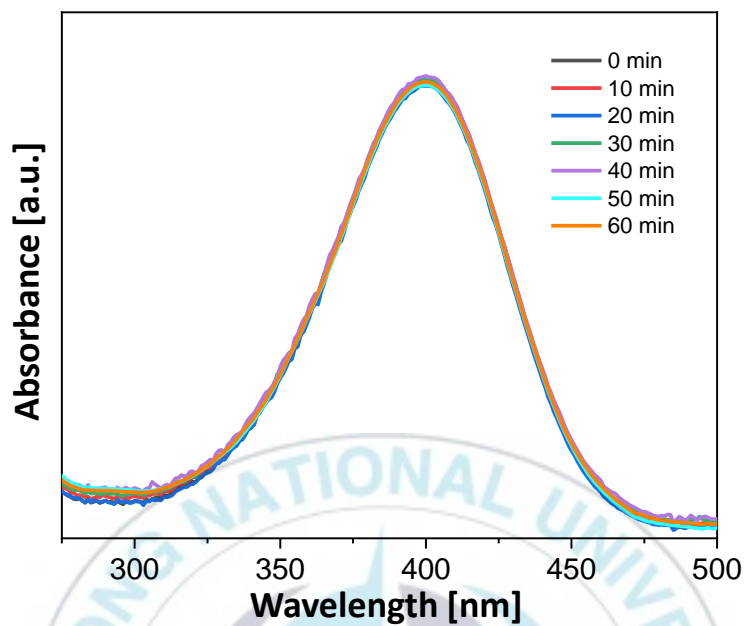


**Figure II. 23** UV-Vis absorption spectra recorded at 10 min intervals for 60 min after Cu microplates were added to the solution containing 4-NP and NaBH<sub>4</sub>.

**Table II. 2** Values of the activity parameter,  $\kappa$ , for various heterogeneous catalysts; the values of  $k$  were obtained by dividing the reaction rate constant by the total weight of used catalyst

| Catalyst                        | Total weight of used catalyst [mg] | Reaction rate constant ( $k$ ) [ $10^{-3} \text{ s}^{-1}$ ] | $\kappa$ [ $\text{s}^{-1}\text{g}^{-1}$ ] | Ref.             |
|---------------------------------|------------------------------------|---|---|------------------|
| Cu nanoparticles                | 13                                 | 1.54  | 0.12                                      | [30]             |
| Hierarchical Cu microspheroids  | 4                                  | 3.99  | 1   | [110]            |
| CuO nanoparticles               | 12                                 | 15.97   | 14.6                                      | [111]            |
| CuO nanosheets                  | 01                                 | 4.58  | 45.8                                      | [31]             |
| Cu cubes                        | 0.096                              | 5.7   | 60  | [51]             |
| Porous microspheres             | 0.06                               | 4.29  | 71.5                                      | [112]            |
| Cu nanoplates                   | 0.07                               | 9.5   | 136                                       | [113]            |
| <b>Cu–Au hybrid microplates</b> | <b>0.07</b>                        | <b>11.6</b>   | <b>166</b>                                | <b>This work</b> |

## II.4 Conclusions

In summary, we developed an easy-to-use and rapid synthesis method to prepare Cu microplate-based hybrid heterostructures with unique nanoarchitectures, high stability, and good catalytic activity. A well-defined, kinetically controlled synthetic method capable of producing Cu microplates in the presence of acetonitrile was developed. Here, acetonitrile served as a ligand to form a complex with Cu(II) ions, and this coordination substantially lowered the reduction rate of Cu(II) ions, enabling the formation of Cu microplates in high yield. Cu@Cu<sub>2</sub>S metal–semiconductor hybrid microplates were synthesized by reacting the Cu microplates with an aqueous Na<sub>2</sub>S solution under ambient conditions. The Cu@Cu<sub>2</sub>S hybrid microplates showed excellent photocatalytic activity when used as a photocatalyst for MB degradation under sunlight irradiation and could be reused several times without substantial loss of photocatalytic activity. Through a galvanic replacement reaction, Cu microplates were transformed into Cu–Au bimetal microplates having rough surfaces with open nanocavities. When used as catalysts for the hydrogenation of 4-NP by NaBH<sub>4</sub>, the Cu–Au hybrid microplates showed high catalytic activity because of their unique surface structure and binary alloy composition; they also exhibited good reusability. We believe that the aqueous solution-based hybridization routes developed in the present study can provide useful platforms for the fabrication of Cu-based nanocatalysts with the potential to replace noble metals in a wide range of catalytic applications.

## **Chapter III.**

# **Facile Synthesis and Sulfidation of PdAuAg Ternary Nanostructures and Their Photocatalytic Applications**



### III.1 Introduction

Noble-metal nanoparticles are gaining popularity as a result of their potential applications in catalysis, sensing, electronics, and bioimaging [39, 57, 114-116]. The optical features of noble-metal nanostructures, - so called localized surface plasmon resonance (LSPR), are used in the majority of these applications. At a given resonance wavelength of the incident light, this LSPR is coupled with charge density oscillation within the particles, resulting in strong electromagnetic field confinement around the nanoparticle [3,12]. The location, intensity, and type of LSPR are all highly dependent on the material, shape, size, composition, dielectric environment, and local refractive index near nanoparticles [12,38]. The location and strength of LSPR bands in Ag and Au nanocrystals, for instance, are highly correlated with the particle shape [117-118]. Controlling noble metal nanocrystals is thus very desirable and necessary for improving performance in many applications.

Hybrid nanostructures / multi-metallic nanoparticles have recently drawn attention due to their unique set of enhanced features that distinguish them from monometallic nanoparticles [15, 17, 58]. Galvanic replacement reaction, seed-mediated growth, and electrodeposition have been used to prepare hybrid metal nanostructures. However, the seed-mediated growth method has been more efficient to synthesize a facile and convenient hybrid nanostructure. Even more, by not involving harmful organic reagents, the seed-mediated method with a water-

based approach provides a more environmentally friendly and convenient way to make hybrid metal nanocrystals. Among the as-prepared seed, a primary seed of pd-based nanocrystals is commonly used due to the excellent catalytic properties of Pd [119 - 120]. In seed-mediated growth, when the deposited metal and the seed have chemical differences, it is heterogeneous; otherwise, it is homogeneous. Many factors influence nanostructure growth, including kinetics, thermodynamics, capping agent, and foreign ions. For instance, foreign ions, particularly  $\text{Ag}^+$  ions, are commonly utilized to influence the formation of Au nanostructures [121]. Although the impact of  $\text{Ag}^+$  ions on the formation of Au nanostructures remains unclear [122], nonetheless this method works well for achieving controlled growth of noble metal nanostructures.

Because of the combination of qualities between single metal and second/third metal, hybrid nanostructures have shown greater catalytic activity than monometallic nanoparticles in the field of catalysis. Regarding this, some multi-metallic nanocatalysts have been employed such as core-shell  $\text{Al}_2\text{O}_3@\text{AgAu}$ , Cu-Ni-Pt dendrites, core-shell  $\text{Au}@\text{Pd}@\text{Ru}$ , and Au/PtPd core/shell for reduction of pollutants, hydrogenation reaction, and organic Suzuki coupling reaction [123-126]. As we know, textile, paper, food, cosmetics, and other dyes are a major source of water pollution because they produce colorful effluent that is loaded with hazardous species. Decolorization of those dyes in wastewater can be achieved by photodegradation. Although there have been several reports of the utilization of Pd

as a catalyst, hybrid metal-semiconductor catalyst with both facile and fascinating morphology of the ternary metal (involving Pd) with semiconductor material is still limited. Therefore, the strategies to make hybrid nanostructures would enable enhancing their stability and excellent synergistic properties from the metal and semiconductor components.

Herein, through site-selected growth of Au on Pd nanoplate seeds, we established a seed-mediated strategy for the production of PdAuAg nanostructures. Due to their larger surface free energy, the initial growth positions are near the edge and vertices. The presence of  $\text{AgNO}_3$  in the system also played a role in the formation of highly homogeneous PdAuAg nanostructures. Furthermore, rapid sulfidation processes involved reactions between PdAuAg nanostructures with sulfur species from sodium sulfide. This rapid sulfidation reaction successfully produces hybrid metal-semiconductor, PdAuAg-AuAgS hybrid nanostructures. The whole growth route for the synthesis of PdAuAg-AgAuS hybrid nanostructures were illustrated in Figure III.1. By taking the advantage of these materials, the catalytic activity of both PdAuAg and PdAuAg-AuAgS nanostructures towards the reductive degradation of methylene blue (MB) was investigated in this study to see how altering the metal to a hybrid metal affects the catalytic properties. Pure Pd has been tested as monometallic nanocatalysts as well. PdAuAg-AuAgS hybrid nanostructures exhibit the best catalytic activity in photocatalysis relative to the

other nanocatalysts; Pd nanoplates and PdAuAg nanostructures, with the same model reaction.

## **III.2 Experimental**

### **III.2.1 Chemicals and Materials**

Sodium tetrachloropalladate ( $\text{Na}_2\text{PdCl}_4$ ), citric acid, hydroxylamine hydrochloride ( $\text{NH}_2\text{OH}\cdot\text{HCl}$ ), polyvinylpyrrolidone (PVP;  $M_w \approx 10$  kDa), silver nitrate ( $\text{AgNO}_3$ ) and gold (III) chloride trihydrate ( $\text{HAuCl}_4\cdot 3\text{H}_2\text{O}$ ) were purchased from Sigma-Aldrich (USA). Sodium sulfide nonahydrate ( $\text{Na}_2\text{S}\cdot 9\text{H}_2\text{O}$ ) was purchased from Acros Organics (USA). Methylene blue (MB) was obtained from Junsei Chemical (Japan). Chemicals were used without further purification, and deionized (DI) water was used for all reactions.

### **III.2.2 Synthesis of Pd Nanoplates**

The Pd nanoplates were prepared using a previously reported method [127]. In a typical synthesis of Pd nanoplates with an average size of 42 nm, an aqueous solution containing 0.1 g PVP ( $M_w \approx 55$  000, Aldrich) was dissolved in 7.45 ml of distilled water. Then, 50  $\mu\text{L}$  of aqueous hydroxylamine hydrochloride (30 mM, Aldrich), 0.5 mL of aqueous citric acid (100 mM, Aldrich), and 1 mL  $\text{Na}_2\text{PdCl}_4$  (12 mM, Aldrich) were added to the solution and a yellow (color of Pd(II) solution) were obtained. The mixture was heated at 100°C in an oil bath without stirring. After 3 h, the obtained solution was brown which indicated the formation of

palladium nanoparticles, was collected by centrifugation and washed with DI water at 13,000 rpm for 30 min. The Pd nanoplates were dispersed in DI water with a final concentration of 0.9 mg/mL.

### **III.2.3 Synthesis of PdAuAg Nanostructures**

The PdAuAg nanostructures were prepared following the seed-mediated growth method. 0.3 g PVP 55 kDa was dissolved in 5 mL of DI water, subsequently, 100  $\mu$ L of Pd seed was diluted to the PVP solution. This solution was heated (100°C) under stirring for 10 min. Then, 150  $\mu$ L of a mixed aqueous solution of H<sub>2</sub>AuCl<sub>4</sub> and AgNO<sub>3</sub> (10 mM: 10 mM) was added to the vial through a syringe pump at a rate of 45 mL h<sup>-1</sup>. The mixture was heated for two hours and left to cool to room temperature. The product was collected by centrifugation (13,000 rpm, 8 min) and washed several times with deionized water for further experiments.

### **III.2.4 Sulfidation Reaction**

For the synthesis of the metal-semiconductor PdAuAg-AuAgS nanostructures, 0.2 g of PVP 55 kDa was dissolved in 4 ml DI water. Subsequently, 0.5 mL of the as-prepared PdAuAg dispersions and 500 mL of aqueous Na<sub>2</sub>S solution (100 mM) were injected into the above solution. The reaction was allowed to proceed under vigorous stirring at room temperature for 30 min. Finally, the color changed from purple to a grey color indicating the PdAuAg-AuAgS hybrid nanostructures were

obtained. The product was collected by centrifugation at 13,000 rpm for 8 min several times and redispersed in 1 mL DI water.

### **III.2.5 Photocatalytic Activity**

To investigate the photocatalytic activity of the as-prepared PdAuAg and PdAuAg-AuAgS nanostructures, the methylene blue photodegradation was examined by the addition of the nanocatalyst solution. The reduction of the dye was then monitored spectrophotometrically at 664 nm via a measurement of its absorbance with time. The photocatalytic activities of the degradation of MB were evaluated under simulated solar irradiation using a Xe lamp, and the solar irradiation was adjusted to 100 mW/cm<sup>2</sup> and the decrease in absorbance of dye was recorded in a 1 cm quartz cell. The reaction mixture consisted of 4 mL of MB aqueous solution, - and 100  $\mu$ L of the nanocatalyst solution (0.7 g/L). The absorbance of the aqueous solution was measured at the ambient temperature using UV-Vis spectroscopy to investigate the photocatalytic performance during reaction time (30 min).

### **III.2.6 Characterization**

Transmission electron microscopy (TEM; Hitachi H7500) at an acceleration voltage of 80 kV was used to obtain TEM images of nanostructures. X-ray diffraction (XRD) patterns were obtained using a powder X-ray diffractometer (X'Pert3, PANalytical). Field-emission transmission electron microscopy (JFE-TEM, EM-2100F, Jeol), elemental mapping analysis, and high-resolution

transmission electron microscopy (HR-TEM) were conducted. Scanning electron microscopy (SEM) analysis was conducted using a field-emission scanning electron microscope (JSM-6700F, JEOL). X-ray photoelectron spectroscopy (XPS) was carried out using an Axis Nova spectrometer (Kartos Axis Nova, UK). A Cary 50 spectrophotometer (Agilent Technologies, USA) was used to acquire UV–Vis–NIR spectra.



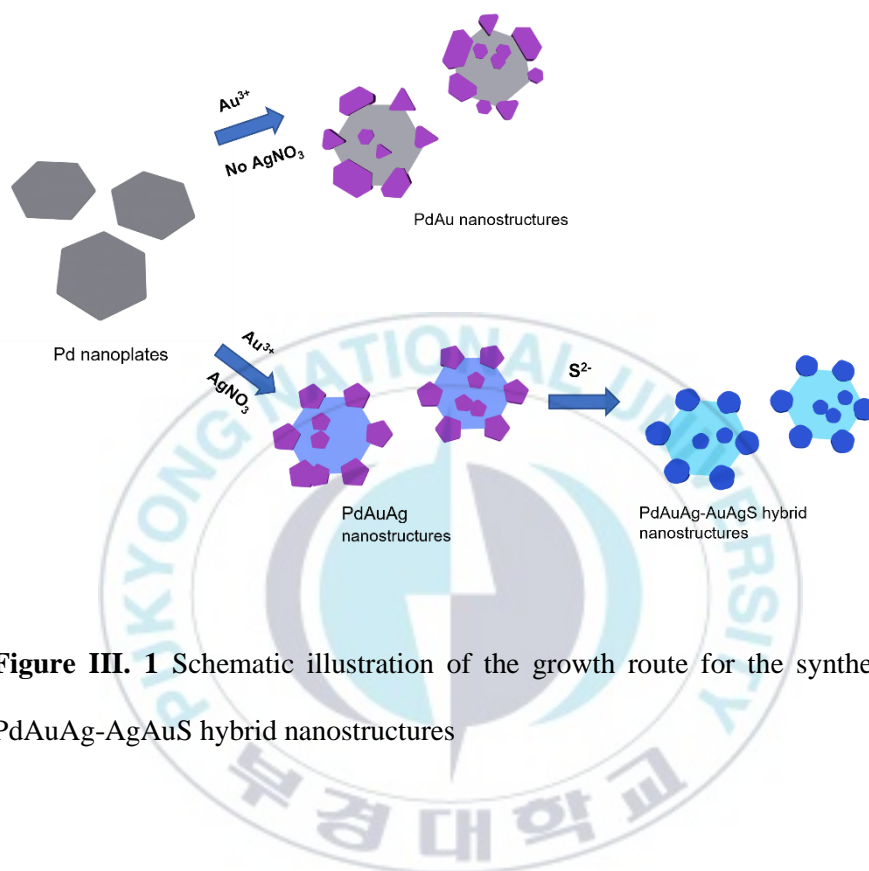


**Figure III. 1** Schematic illustration of the growth route for the synthesis of PdAuAg-AuAgS hybrid nanostructures

### III.3 Result and Discussion

The synthesis of Pd seed was conducted in an aqueous solution containing  $\text{Na}_2\text{PdCl}_4$ , hydroxylamine hydrochloride, citric acid, and PVP at  $100^\circ\text{C}$ .  $\text{Na}_2\text{PdCl}_4$ , hydroxylamine hydrochloride and PVP served as a precursor to elemental Pd, reducing agent, and colloidal stabilizer, respectively. Citric acid served as capping agent since citrate ion is served as a capping agent towards Pd (111) facets along with the  $\text{Cl}^-$  from  $\text{Na}_2\text{PdCl}_4$ . The change in color of the solution from light yellow to deep brown in the first thirty minutes of the reaction indicates the formation of Pd nanocrystals. A typical TEM image and Uv-Vis spectrum of Pd nanoplates in an aqueous solution are shown in Figure III.2(A) and 2(C), respectively. Most of the nanoplates have a hexagonal, truncated triangular shape and a few are irregular polygons. The optical response of palladium nanoparticles commonly shows between 200 and 600 nm. The spectrum of Pd nanoplates contains a low absorption peak at 238 nm due to the surface plasmon resonance of Pd which has lower conductivities at an optical frequency than Au or Ag. The SPR properties of metal nanostructures are tunable depending on their size. Herein, by tuning the sizes of Pd nanoplates by changing the concentration of citric acid, different-sized Pd nanoplates with SPR peaks intensity were readily prepared (Figure III.3). Pd nanoplates with an average edge length of 42 nm were selected for further experiments. Moreover, TEM images of nanoplates taken along different zone axes exhibit a plate-like morphology with a length of 42 nm and thickness of 8 nm in

Figure III.2(A) and 2(D), respectively. The fast fourier transform (FFT) pattern (Inset of Figure III.2(B)) displayed the incident electron beam was directed perpendicular to one hexagonal facet of an individual nanoplate, and one pair of diffraction spots could be indexed as the (220) and (422) reflections, respectively, demonstrating that the two hexagonal facets were bordered by the {111} facets. More detailed information, the enlarged HR-TEM images of Pd nanoplates in the Figure III.2(B) observed that the lattice fringes are about 0.22 nm were assigned to Pd(111). The XRD pattern (Figure III.4) also proves its crystalline nature of face-centered cubic (fcc) structure, and the peaks match well with standard Pd reflections (JCPDS No. 05-0681) [129]. Pd nanoplates are composed of (111), (200), (220) and (311) planes with diffraction peaks at about 40, 46, 68, and 82°, respectively.

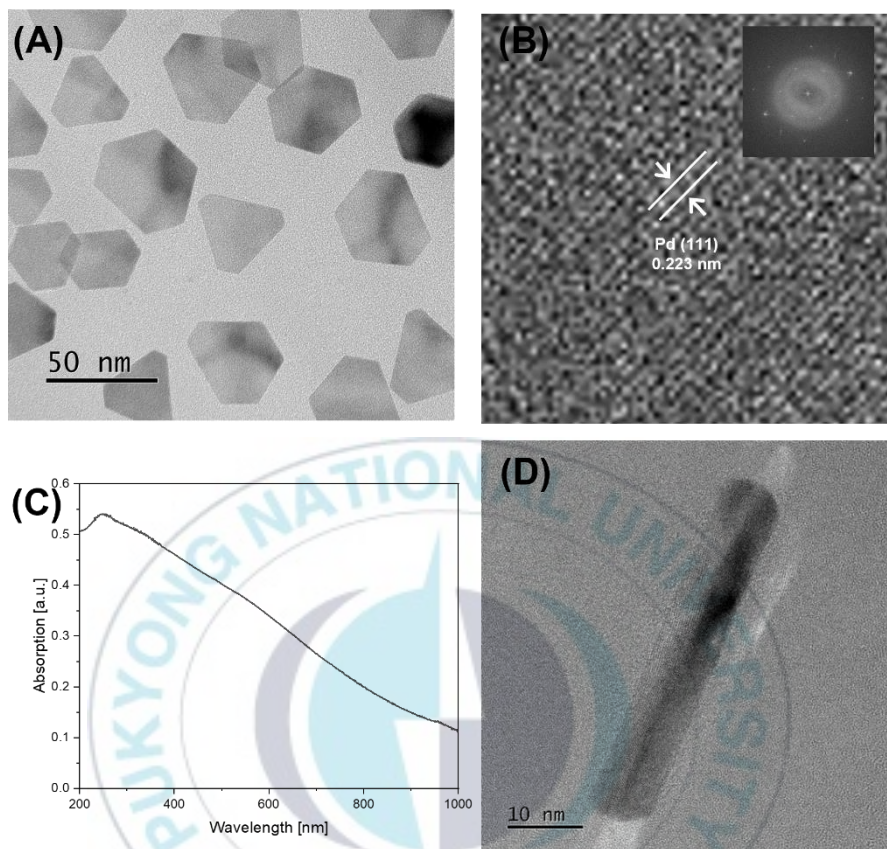


**Figure III. 2** (A) TEM image, (B) High-resolution TEM image (Inset: FFT patterns), (C) UV-Vis-NIR spectrum of the Pd nanoplates. (D) TEM image of vertically lying nanoplates

In a typical synthesis of PdAuAg nanostructures, as-synthesized Pd nanoplates with an average length of 42 nm and a thickness of 8 nm were selected as seeds for the formation of PdAuAg nanostructures. The overgrowth of Au and Ag on Pd nanoplates was achieved by chemically reducing  $\text{HAuCl}_4$  and  $\text{AgNO}_3$  with PVP in an aqueous solution, with Au : Ag molar ratio of 1:1 (10 mM : 10 mM). As shown in the representative transmission electron microscopy (TEM) image in Figure III.6(A), the as-made PdAuAg nanostructures had an average length of = 54 nm, larger than that of Pd nanoplate seeds. Furthermore, the average length of the Au nanocrystals both at the edge and basal site of Pd nanoplates is  $\sim 8$  nm. A lattice mismatch of 4.7% for Pd/Au and Pd/Ag plays a critically important role in the overgrowth of the secondary metal and a high lattice mismatch prevents the conformal overgrowth. To confirm the formation of the Pd nanoplates supported AuAg nanocrystals prepared using the standard procedure, the HR-TEM and HAADF-STEM, and XRD characterizations were employed. The images of individual nanostructures revealed that the fringes with a lattice spacing of 0.23 and 0.20 nm can be attributed to the  $\{111\}$  and  $\{200\}$  facets of Au with a face-centered cubic structure, respectively. The Au nanocrystals tend to assemble into an ordered polyhedral array on Pd nanoplates. Furthermore, the elemental-mapping analysis showed Au atoms were mostly distributed throughout the edge of as-prepared Pd nanoplates, suggesting that Au was successfully selectively grown on the Pd nanoplates. In addition, Ag is mainly located at the epitaxial site of Pd

nanoplates. Enlarged HR-TEM images of the yellow box in Figure III.6(B)-6(C) clearly showed the polyhedral shape with clearly twin boundaries (marked by the blue dashed line) bound by [111] planes. It can be concluded that the twin defect of the polyhedral Au was well preserved despite the overgrowth on the twin boundaries. These observations explicitly validated that multiple-twinned Au polyhedral were successfully synthesized over Pd nanoplate seeds.

To determine the phase structure of these PdAuAg nanostructures, the products were characterized by X-ray diffraction (XRD). As can be seen in Figure III.4, the XRD patterns of all the colloidal PdAuAg nanostructures exhibit typical fcc crystalline features. The XRD pattern of PdAuAg nanostructures showed the characteristic peaks of Au ( $2\theta = 38.1, 44.3, 64.6, \text{ and } 77.5^\circ$ ) and Pd ( $2\theta = 40.1, 46.6, 68.1, \text{ and } 82.1^\circ$ ). Since Ag has a slightly different atomic radii and lattice constant with Au, the peak position of both Au and Ag elements overlap. The single-phase peaks are not observed between the expected diffraction peaks from pure bulk Pd and AuAg. These phenomena are indicative of a heterogeneous mixture of Pd and AuAg.

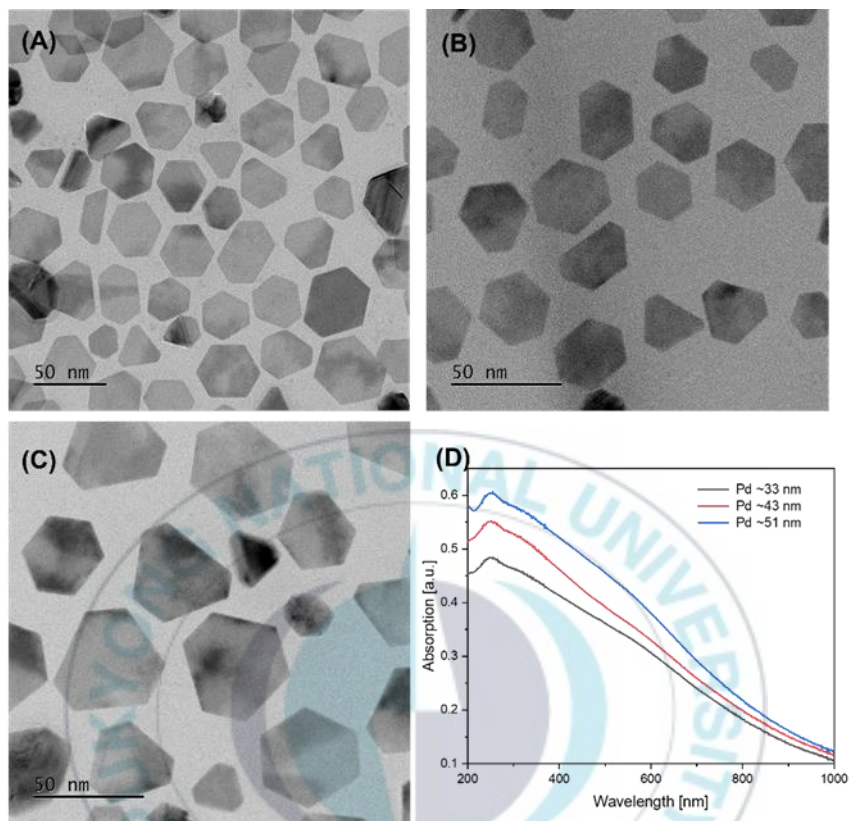


**Figure III. 3** TEM images of Pd nanoplates formed at different amounts of citric acid: (A) 1 mL, (B) 0.5 mL, and (C) 0.25 mL

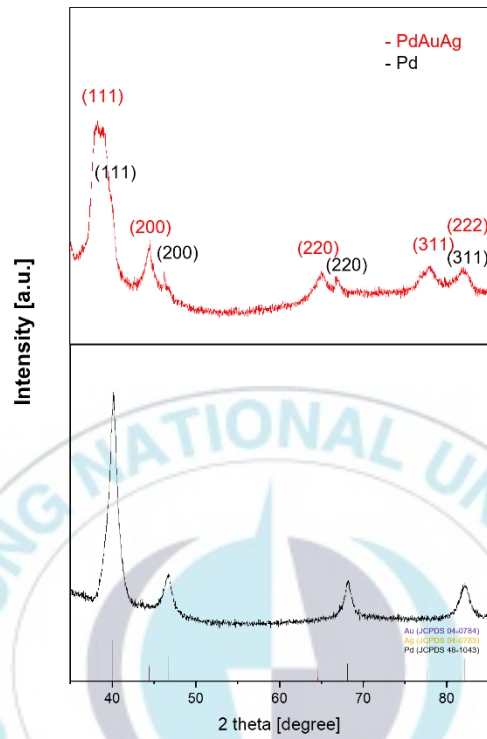


**Figure III. 4** X-ray diffraction pattern of Pd nanoplates and PdAuAg nanostructures.

To decipher the formation mechanism of the AuAg nanocrystals on Pd nanoplates, the TEM images of the samples of the reaction product at specific time points are presented (Figure III.5). After reducing  $\text{HAuCl}_4$  and  $\text{AgNO}_3$  with PVP for 10 seconds, small Au nanocrystals with a size of about 6 nm were obtained, and they were mostly selectively deposited at the corner and edge sites of the Pd nanoplates seeds, which ascribed to the high surface energy of such sites and grew very quickly during the first minute of the reaction. By running the reaction for only one minute, the conversion of  $\text{Au}^{3+}$  into  $\text{Au}^0$  was proceeded as the solution also start to change to purple color. Another insight into how PdAuAg nanostructures arose comes from a closer look at the TEM picture of the 10 s time point (Figure III.5(A)). Instead of adding to Pd nanoplates, some Au nanoparticles homogeneously nucleated to form tiny particles in the reaction solution, as pointed by black arrows. The formation of PdAuAg nanostructures with anisotropic morphology is evident in the time-elapsd extinction spectra recorded from the reaction mixture (Figure III.5(D)), - since Au nanocrystals have unique surface plasmon resonance. At  $t = 10$  s, the extinction spectra of the PdAuAg nanostructures revealed a plasmon band approximately at 538 nm. The intensity of the plasmon band increased as the reaction time proceeded. Due to the fact that Pd has a higher imaginary dielectric constant than Au and Ag, the PdAuAg nanostructures tend to suffer from greater plasmon damping than the counterparts made of low amount of Au, resulting in lower plasmon resonance intensity.

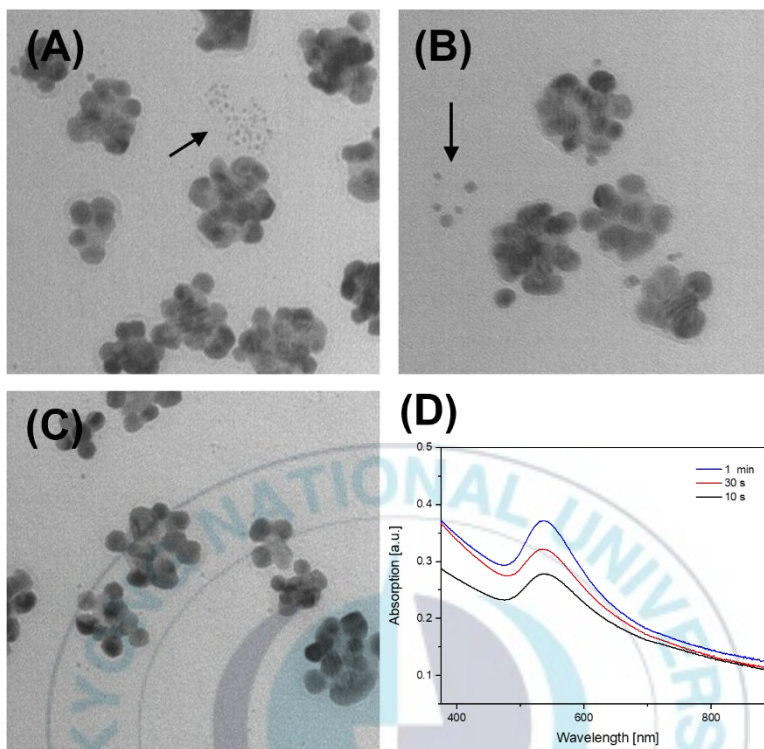


**Figure III. 5** PdAuAg nanostructures TEM images obtained at the reaction after (A) 10 s (B) 30 s and (C) 1 min. (D) UV-Vis spectra of the reaction solution at different times.

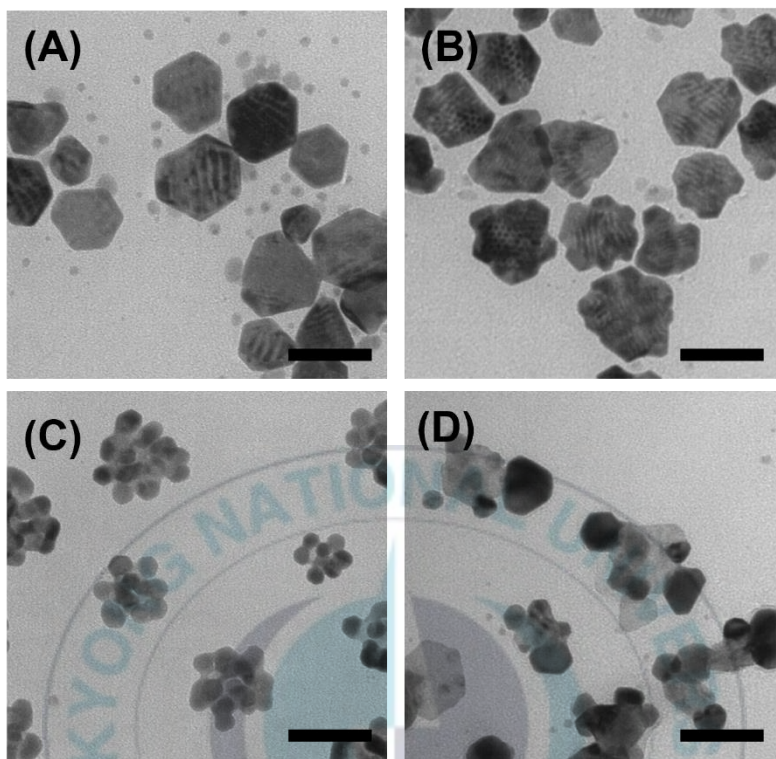


**Figure III. 6** TEM images of PdAuAg nanostructures derived by running the reaction with (A) PVP 10 kDa (B) PVP 29 kDa (C) PVP 55 kDa and (D) PVP 360 kDa. Scale bar = 50 nm.

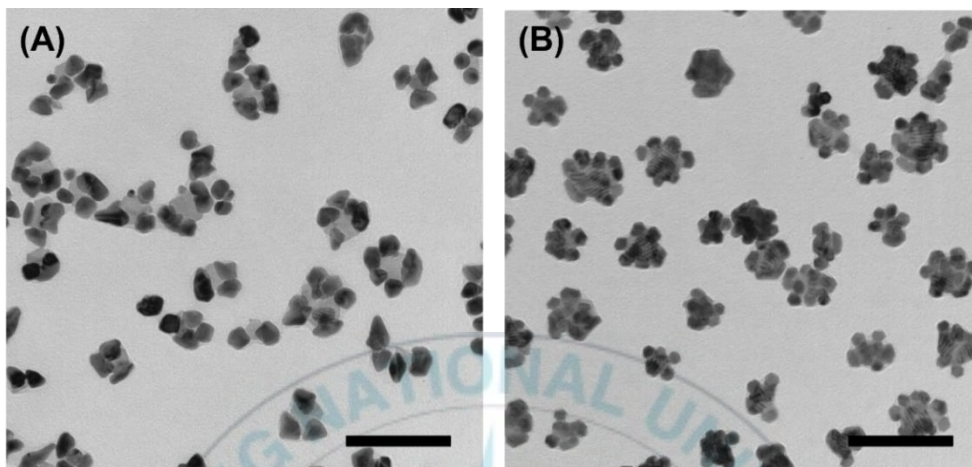


**Figure III. 7** TEM images of PdAuAg nanostructures obtained at (A) room temperature and (B) 100°C. Scale bar = 100 nm

Moreover, PVP and reaction temperature are both important factors in the production of AuAg nanocrystals on Pd nanoplates. In our system, the reduction kinetics could be controlled by varying the molecular weight of PVP. The reduction rate increased if the PVP hydroxyl end groups of a shorter chain of PVP served as a reductant in the system [10]. As a preliminary test, we performed a reaction with PVP 10 kDa, PVP 29 kDa, PVP 55 kDa, and PVP 360 kDa with the expectation that with the use of a shorter chain, the degree of supersaturation for Au atoms increased rapidly due to the fast reduction of  $\text{HAuCl}_4$  precursor by a short chain of PVP. With PVP 10 kDa, there are many small Au particles remaining in the solution after running the reaction for 2 h (Figure III.6(A)). In this situation, the Pd seeds may not be enough to accommodate all of the Au atoms produced by the reduction, causing supersaturation to remain high and encouraging nucleation in the solution. As a result, Au atoms that were unable to nucleate on the surface of Pd seeds self-nucleate to generate new particles. The number of small Au particles rapidly decreased and completely deposited on the Pd nanoplate when the molecular weight of PVP 55 kDa was employed. Another possible explanation for PVP's function has been proposed: parts of the PVP polymer chain that are not linked to the seed's surface grab the  $\text{Au}^{3+}$  ion. PVP's presence effectively enhances its binding affinity for Au particles, increasing the likelihood of the seed colliding with Au particles. On the other hand, the viscosity of the reaction mixture was highly increased with the use of PVP 360 kDa causing a very slow reaction and

cannot proceed homogeneously to the entire reaction mixture. Thus, the irregular shapes formed as a result (Figure III.6(D)) In addition, we also study the effect of temperature on the reaction. It is widely known that high temperatures promote nucleation whereas low temperatures promote nanoparticle growth. At the initial stage of reaction, the Pd seed solution was prepared at 100°C. When the reaction continues at 100°C after the addition of AgNO<sub>3</sub> and HAuCl<sub>4</sub>, the reduction rate increases and the formation of AuAg structures is thermodynamically favored. Adatoms prefer to remain in their original location and are thought to migrate quickly during the formation of nanocrystals, and this migration could influence the shape of the final product. When the reaction temperature is lowered to room temperature after the addition of AgNO<sub>3</sub> and HAuCl<sub>4</sub>, the adatoms tend to migrate to energetically least active regions, resulting in bigger Au particles deposited at the edges of Pd nanoplates. Regarding the effect of reaction temperature, the above results revealed that the size of nanoparticles could become smaller with the increased temperature.

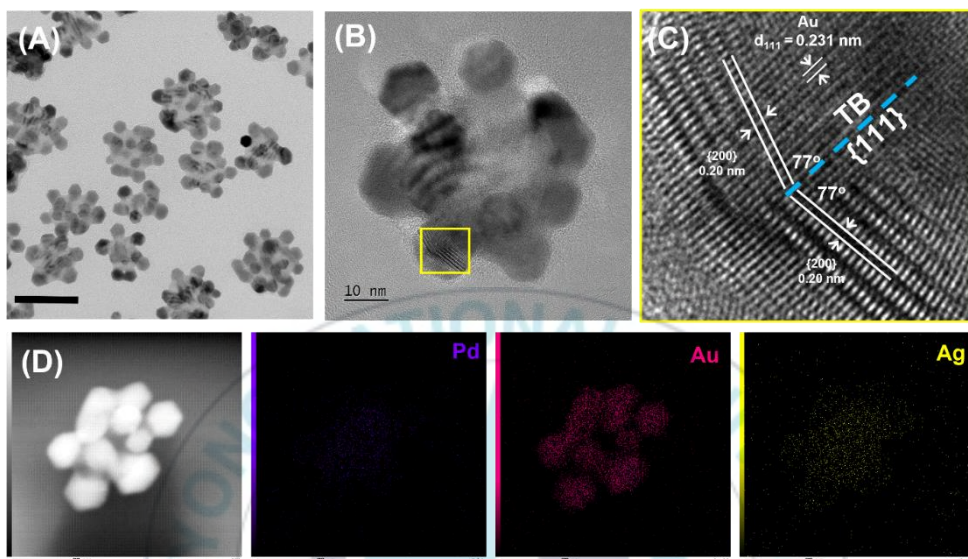
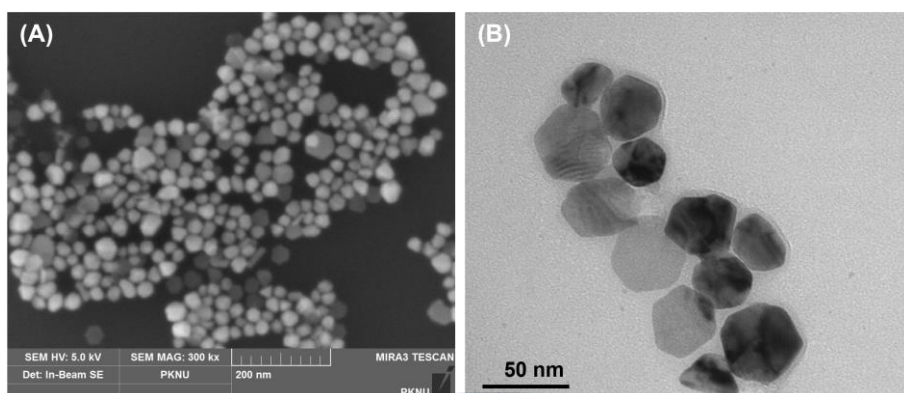


**Figure III. 8** (A) TEM and (B) HR-TEM images of PdAuAg nanostructures. (C) An enlarged image of the yellow box in (B) showed the twin boundaries were obtained. (D) STEM images and elemental mapping of such elements of PdAuAg nanostructures.

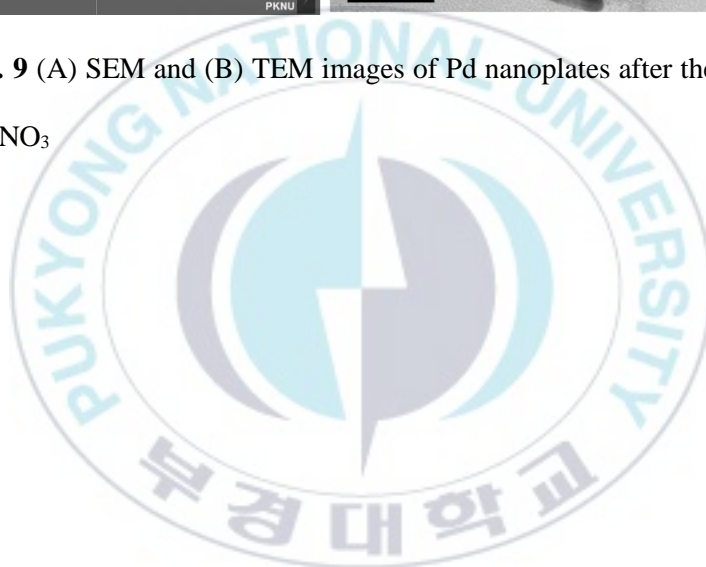
Nanoparticles are frequently circumscribed by three low-index facet types ( $\{111\}$ ,  $\{110\}$ , and  $\{100\}$ ). Their surface free energies differ, with  $E\{110\} > E\{100\} > E\{111\}$  being sequence. The final product must always be constrained by inactive facets to achieve energy reduction. As a result, the rate of growth on a facet with a high surface free energy is faster than on a facet with a low surface free energy. In reality, Pd nanoplates have  $\{111\}$  facets on their front faces and small  $\{100\}$  facets on their side face. Because  $E\{100\}$  is larger than  $E\{111\}$ , the growth along  $\langle 100 \rangle$  should theoretically be the fastest.

The role of  $\text{Ag}^+$  ions on anisotropic growth and the final shape of PdAuAg nanostructures was essential in our system. The presence of  $\text{Ag}^+$  ions is known to be essential for the initiation and control of the anisotropic growth of other noble metal nanostructures. The control experiment, which was conducted without  $\text{AgNO}_3$  but under identical conditions as the regular process, backs up this assertion (Figure III.10). As observed, Au nanostructures grow along the edge of the Pd corner with heterogeneous structures. Although the precise involvement of  $\text{Ag}^+$  ions in the synthesis of PdAuAg nanostructures is unclear, we can see a significant difference between the final products formed with and without  $\text{Ag}^+$  ions. The underpotential deposition of the Ag sub-monolayer on a specific set of facets and the facet specific capping effect of the Ag-complex have been presented as possible processes to account for Ag's function. The inclusion of  $\text{Ag}^+$  ions has long been known to control the development of Au nanocrystals by altering reaction

kinetics via underpotential deposition (UPD) [130]. To further investigate the role that  $\text{Ag}^+$  ions play in the generation of the PdAuAg nanostructures, an additive control experiment was conducted in the absence of  $\text{HAuCl}_4$  with other conditions being the same as in the standard procedure. As shown in Figure III.9, the Pd nanoplates are observed to remain intact with an increase in thickness. This result indicates that  $\text{Ag}^+$  ions deposit on the epitaxial and periphery of Pd nanoplates (core-shell structure). Because  $\text{Ag}^+$  ions do not bind to Pd {100} selectively, they do not affect the distribution of surface free energy in Pd nanoplates. Selective adsorption of  $\text{Ag}^+$  ions on Au {100} facets, on the other hand, results in preferred growth along  $\langle 100 \rangle$ . As a result of their tremendous affinity for Au(100),  $\text{Ag}^+$  ions quickly adsorb on the generated Au(100). As a result, growth along  $\langle 100 \rangle$  becomes slow. Comparatively, the growth along  $\langle 111 \rangle$  is accelerated. These observations indicated that the anisotropic growth of Au depends on  $\text{Ag}^+$  ions introduction in the growth solution. In addition, the introduction of  $\text{AgNO}_3$  promotes a highly uniform PdAuAg nanostructures compared to the absence of this compound in the system.



**Figure III. 9** (A) SEM and (B) TEM images of Pd nanoplates after the addition of 0.01 M  $\text{AgNO}_3$



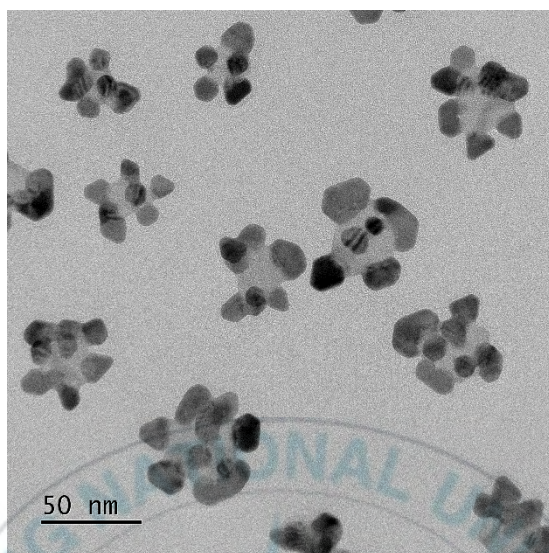


**Figure III. 10** TEM image of PdAu nanostructures (without the presence of Ag<sup>+</sup> ions)

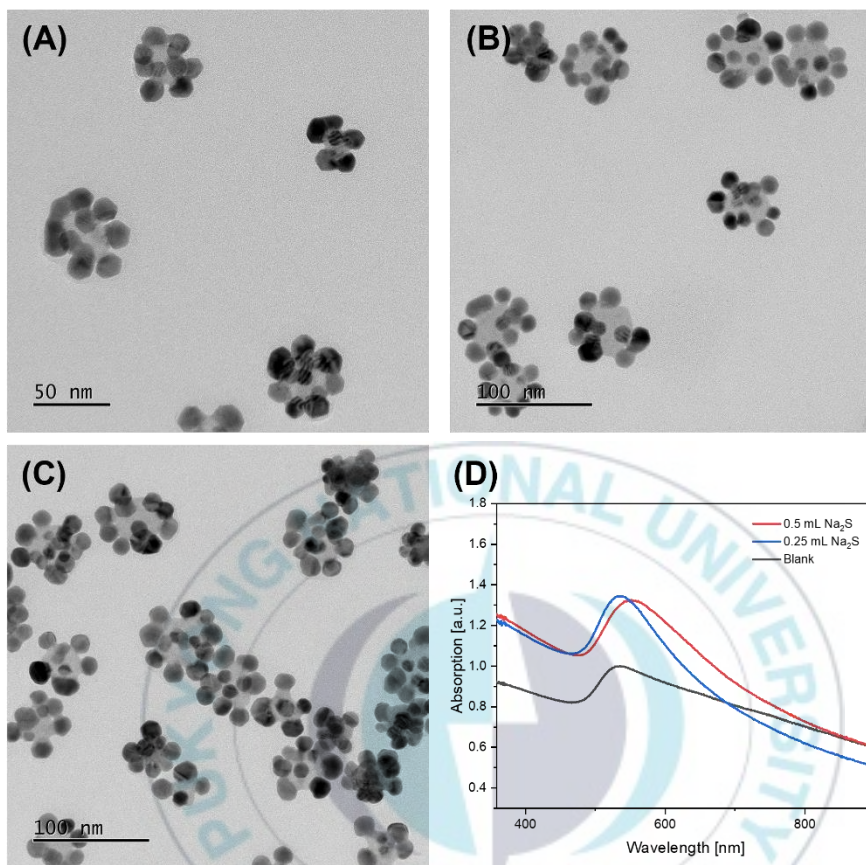
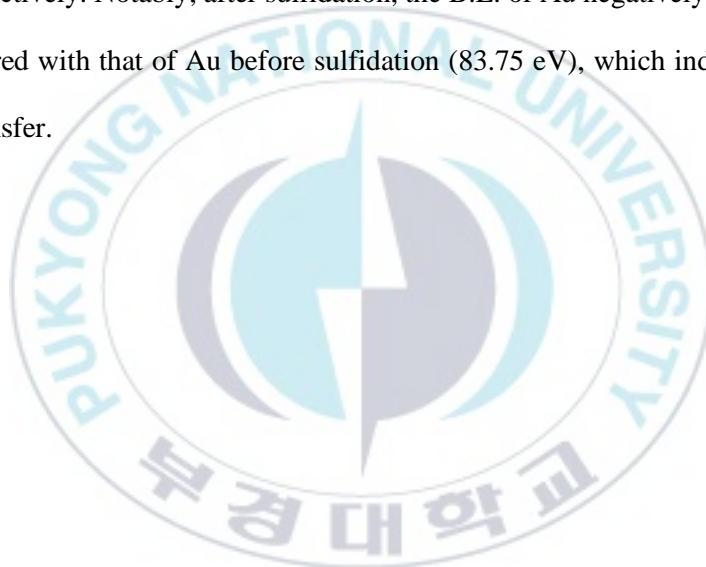


**Figure III. 11** TEM images of (A) PdAuAg nanostructures before and after the reaction with (B) 0.25 mL and (C) 0.5 mL of 100 mM Na<sub>2</sub>S solution.

PdAuAg-AuAgS hybrid nanostructures were prepared by a sulfidation reaction. The as-synthesized PdAuAg nanostructures as the template were mixed with PVP 55 kDa and sodium sulfide ( $\text{Na}_2\text{S}$ ), where  $\text{Na}_2\text{S}$  served as a sulfur source. After sulfidation at room temperature for 30 min, the corresponding aqueous PdAuAg-AuAgS hybrid nanostructures were obtained with a grey black color. By regulating the addition amount of  $\text{Na}_2\text{S}$ , the outer site of PdAuAg-AuAgS hybrid nanostructures is more spherical, indicating the formation of an AuAgS layer covering the Au nanocrystals. Furthermore, once the sulfur coverage increase, semiconductor cover areas on the Au side gradually increase, hence, the corresponding UV-Vis spectra of PdAuAg and PdAuAg-AuAgS nanostructures blueshifts from 538 nm to 554 nm, owing to the reshaping of PdAuAg nanostructures and the sulfide layer growth [131]. Those conclusions are agreed with the HR-TEM results in Figure III.12(B) (d-spacing = 0.277 nm assigned to AuAgS)

The XRD, high-resolution TEM, and STEM characterization have been carried out on PdAuAg-AuAgS hybrid nanostructures. The diffraction peaks from AuAgS displayed in Figure III.12(C) can be well identified according to JCPDS card no. 19-1146. The results reveal that the majority crystalline system of AuAgS components is the monoclinic system (31.6, 34.1, 40.1, and  $51^\circ$  were attributed to (102), (121), (013), and (004) plane, respectively), while the Au components are in the cubic phase. STEM-EDS mapping images show the hexagonal Pd core, Ag

layer, well-defined Au, and sulfur location. All the above results indicate the successful formation of PdAuAg-AuAgS hybrid nanostructures. Furthermore, XPS was also applied to further investigate the elemental valences of these compositions as well as the electronic coupling effect among Pd, Au, and Ag. As for the XPS spectrum of Ag in Figure III.13, the two typical peaks presented at the binding energy (B.E.) of 373.6 eV and 367.63 eV are assigned to metallic Ag(0)  $3d_{3/2}$  and  $3d_{5/2}$ , respectively. Notably, after sulfidation, the B.E. of Au negatively shifted  $\sim 0.1$  eV compared with that of Au before sulfidation (83.75 eV), which indicates slight charge transfer.



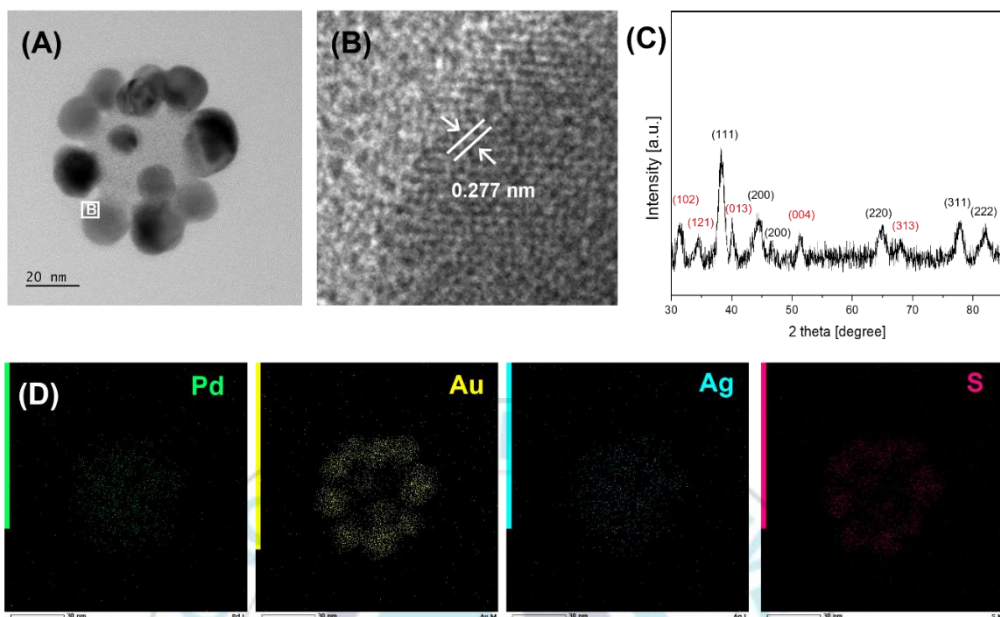


**Figure III. 12** (A-B) HR-TEM images, (C) XRD pattern of PdAuAg-AuAgS hybrid nanostructures acquired by the reaction between PdAuAg nanostructures and  $\text{Na}_2\text{S}$ . (D) STEMEDS elemental mapping images of PdAuAg-AuAgS hybrid nanostructures.

Due to the integrated metal and semiconductor nanocrystals increased interaction between plasmons and excitons, metal-semiconductor hybrid materials are recognized as perfect photocatalysts. Moreover, several polyhedral covered by [111] facets have been rationally and reproducibly prepared in high yields according to this approach. These PdAuAg-AuAgS hybrid nanostructures with high uniformity might find uses in catalysis. Compared with the monometallic nanocrystals, and PdAuAg nanostructures, hybrid-metal of PdAuAg-AuAgS nanostructures, possess a high effective photocatalysts because of their synergistic effect between metal and semiconductor components. To investigate the photocatalytic activity, we carried out photooxidative degradation of the organic dye MB under solar irradiation in the presence of Pd nanoplates, the as-synthesized PdAuAg, or PdAuAg-AuAgS hybrid nanostructures for 30 min. As a result, the intensities of two characteristic absorption peaks of the MB molecules at 664 and 609 nm fall significantly with time. As shown in Figure III.13(A), after 30 minutes of irradiation, the degradation of PdAuAg-AuAgS nanostructures as a photocatalyst was nearly 100%. The normalized maximum absorbance ( $A_t/A_0$ ), which may be calculated from the change in the MB absorption profile over time, is proportional to the temporal concentration changes ( $C_t/C_0$ ) of MB during the photocatalytic process. The photocatalytic reaction can be thought of as a pseudo-first-order reaction since  $\ln(C_t/C_0)$  has a linear relationship with reaction time. The PdAuAg-AuAgS hybrid nanostructures is higher than that of the PdAuAg

nanostructures and Pd nanoplates with the apparent kinetic rate constant ( $K_{app}$ ) were estimated to be  $0.0933 \text{ min}^{-1}$ ,  $0.0378 \text{ min}^{-1}$ , and  $0.0182 \text{ min}^{-1}$ , respectively. From the above result, Pd nanocrystals have already shown excellent application as a catalyst, however, their photocatalytic activity can be remarkably improved through hybridization with semiconducting material.

To evaluate the stability and reusability of the catalysts, additional experiments were conducted. The cycle performance of PdAuAg-AuAgS hybrid nanostructures for the degradation of MB under solar light irradiation showed in Figure III.13(D). The result reveals that the PdAuAg-AuAgS hybrid nanostructures possess good catalytic stability, which remains above 75% in the photodegradation of MB after three cycles. Furthermore, structural characterization of PdAuAg-AuAgS hybrid nanostructures before and after photocatalytic reactions suggests that all nanocrystals and their composition remain unchanged (Figure III.15)

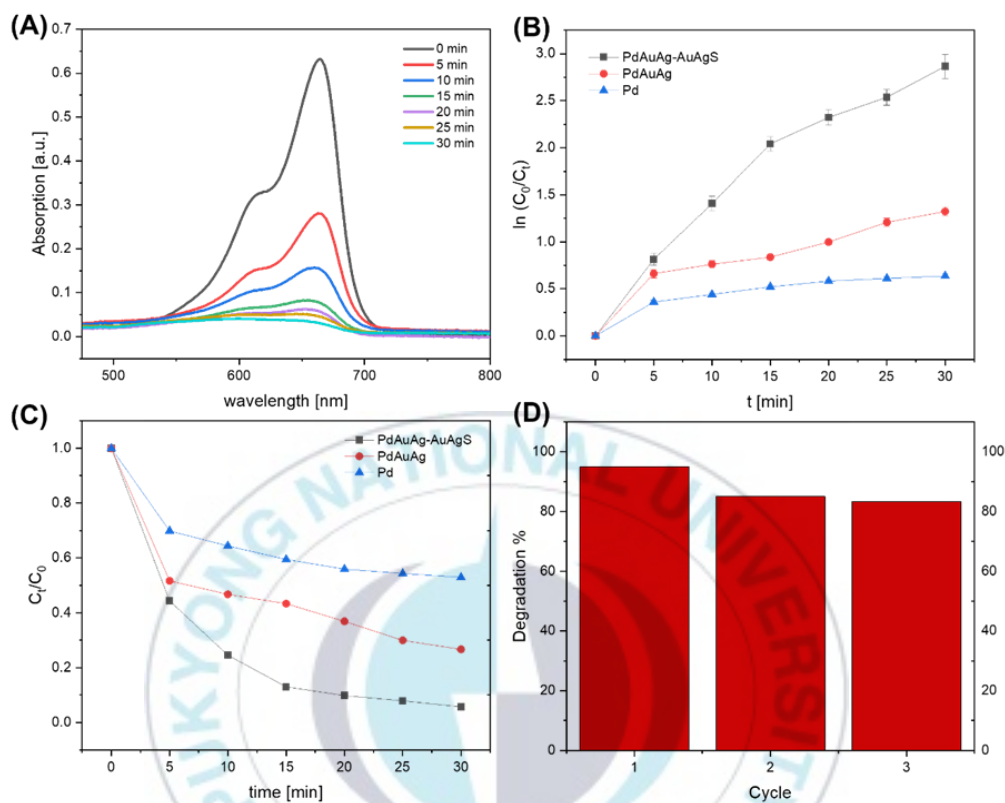


**Figure III. 13** Photocatalytic degradations monitored by (A) the absorption spectra for MB using PdAuAg-AuAgS hybrid nanostructures. (B-C) Photodegradation kinetics of different nanocatalysts; Pd, PdAuAg, and PdAuAg-AuAgS hybrid nanostructures. (D) Recyclability of the PdAuAg-AuAgS hybrid nanostructures as catalysts.

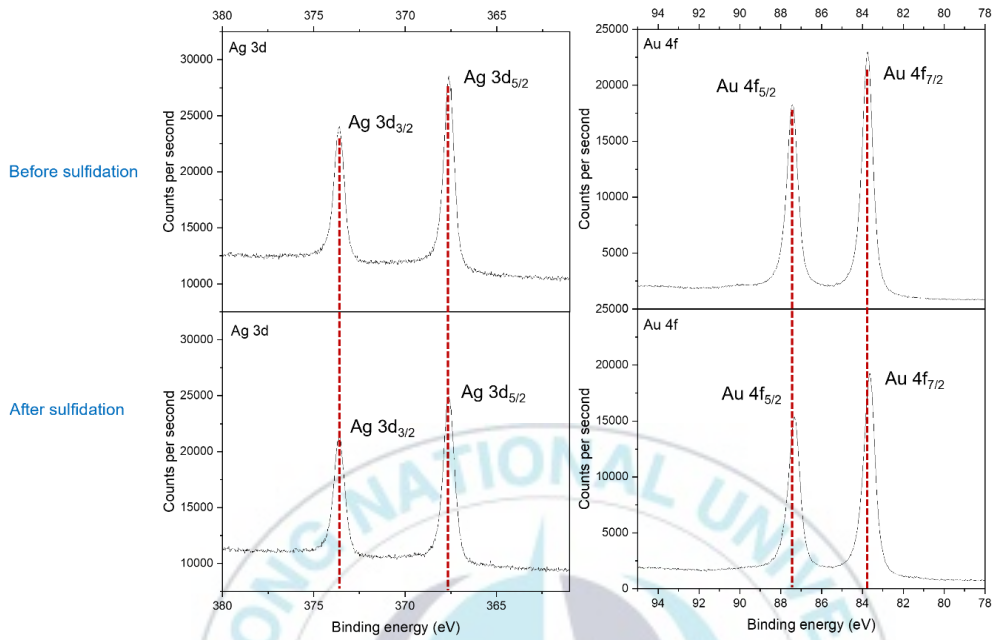


**Figure III. 14** XPS spectra of Ag 3d and Au 4f content for Ag and Au elements of PdAuAg nanostructures obtained before and after introducing Na<sub>2</sub>S solution.

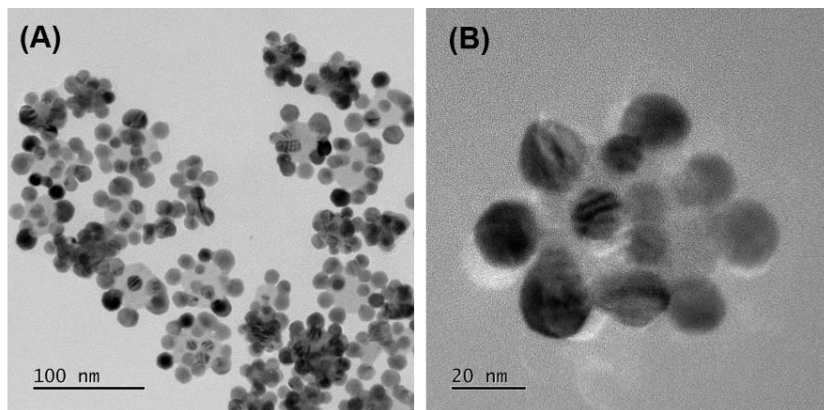
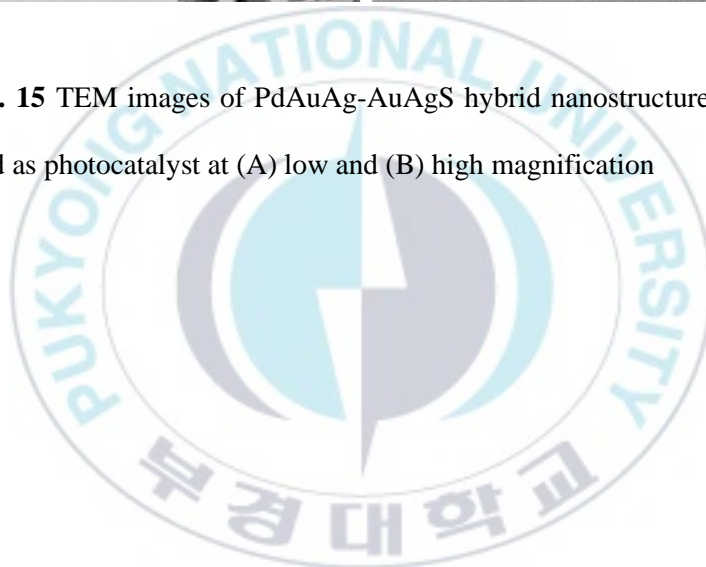


**Figure III. 15** TEM images of PdAuAg-AuAgS hybrid nanostructures after three cycles used as photocatalyst at (A) low and (B) high magnification



### III.4 Conclusions

In summary, we have successfully developed a facile method for the synthesis of heteronanostructures of hybrid metal-semiconductor, PdAuAg-AuAgS nanostructures, for enhancement of catalysis. Our strategy provides the way of using seed-mediated growth to direct selective growth on anisotropic Pd seeds by the following curvature and edge selectively due to higher surface free energy and thus particularly active for the nucleation of Au. Interestingly, the introduction of AgNO<sub>3</sub> in the system promotes a highly uniform PdAuAg nanostructures. The as-synthesis PdAuAg nanostructures were used as a template for the further reaction to make a hybrid metal-semiconductor sample. Na<sub>2</sub>S aqueous solution was introduced to the system and sophisticatedly produce PdAuAg-AuAgS hybrid nanostructures. With the great structural complexity and synergistic properties, the ordered hybrid metal-semiconductor of PdAuAg-AuAgS nanostructures positively affects a photocatalytic performance; enhanced by 40% with metal and semiconductor incorporation on the structure. In addition, these prepared PdAuAg-AuAgS hybrid nanostructures display a good reproducibility, thus we believe this present approach may offer an alternative platform for future development of compatible photocatalyst.

## References

- [1] C. N. R. Rao, G. U. Kulkarni, P. J. Thomas, and P. P. Edwards. “Metal nanoparticles and their assemblies,” (2000)
- [2] P. G. Jamkhande, N. W. Ghule, A. H. Bamer, and M. G. Kalaskar, “Metal nanoparticles synthesis: An overview on methods of preparation, advantages and disadvantages, and applications,” *Journal of Drug Delivery Science and Technology*, vol. 53. Editions de Sante (2019)
- [3] E. S. Kooij, W. Ahmed, H. J. W. Zandvliet, and B. Poelsema, “Localized plasmons in noble metal nanospheroids,” *Journal of Physical Chemistry C*, vol. 115, no. 21, pp. 10321–10332 (2011)
- [4] X. Wang, S. C. Huang, S. Hu, S. Yan, and B. Ren, “Fundamental understanding and applications of plasmon-enhanced Raman spectroscopy,” *Nature Reviews Physics*, vol. 2, no. 5. Springer Nature, pp. 253–271 (2020)
- [5] Y. Xiong and Y. Xia, “Shape-controlled synthesis of metal nanostructures: The case of palladium,” *Advanced Materials*, vol. 19, no. 20, pp. 3385–3391 (2007)
- [6] Y. Xia, Y. Xiong, B. Lim, and S. E. Skrabalak, “Shape-controlled synthesis of metal nanocrystals: Simple chemistry meets complex physics?,”

*Angewandte Chemie - International Edition*, vol. 48, no. 1. pp. 60–103  
(2009)

- [7] I. Khan, K. Saeed, and I. Khan, “Nanoparticles: Properties, applications and toxicities,” *Arabian Journal of Chemistry*, vol. 12, no. 7. Elsevier B.V., pp. 908–931 (2019)
- [8] E. Dinda, S. Si, A. Kotal, and T. K. Mandal, “Novel ascorbic acid based ionic liquids for the in situ synthesis of quasi-spherical and anisotropic gold nanostructures in aqueous medium,” *Chemistry - A European Journal*, vol. 14, no. 18, pp. 5528–5537 (2008)
- [9] K. Sun, J. Qiu, J. Liu, and Y. Miao, “Preparation and characterization of gold nanoparticles using ascorbic acid as reducing agent in reverse micelles,” *Journal of Materials Science*, vol. 44, no. 3, pp. 754–758 (2009)
- [10] M. H. Kim, J. J. Lee, J. B. Lee, and K. Y. Choi, “Synthesis of silver nanoplates with controlled shapes by reducing silver nitrate with poly(vinyl pyrrolidone) in N-methylpyrrolidone,” *CrystEngComm*, vol. 15, no. 23, pp. 4660–4666 (2013)
- [11] K. Khurana and N. Jaggi, “Localized Surface Plasmonic Properties of Au and Ag Nanoparticles for Sensors: a Review,” *Plasmonics*, vol. 16, no. 4. Springer, pp. 981–999 (2021)

- [12] S. Unser, I. Bruzas, J. He, and L. Sagle, “Localized surface plasmon resonance biosensing: Current challenges and approaches,” *Sensors (Switzerland)*, vol. 15, no. 7. MDPI AG, pp. 15684–15716 (2015)
- [13] S. K. Ghosh, S. Nath, S. Kundu, K. Esumi, and T. Pal, “Solvent and ligand effects on the localized surface plasmon resonance (LSPR) of gold colloids,” *Journal of Physical Chemistry B*, vol. 108, no. 37, pp. 13963–13971 (2004)
- [14] Y. Hong, Y. M. Huh, D. S. Yoon, and J. Yang, “Nanobiosensors based on localized surface plasmon resonance for biomarker detection,” *Journal of Nanomaterials*, vol. 2012 (2012)
- [15] D. Semenova, K. v. Gernaey, and Y. E. Silina, “Exploring the potential of electroless and electroplated noble metal-semiconductor hybrids within bio- and environmental sensing,” *Analyst*, vol. 143, no. 23. Royal Society of Chemistry, pp. 5646–5669 (2018)
- [16] A. Pradyasti, D. H. Kim, M. N. Biutty, S. il Yoo, and M. H. Kim, “Ag–Ag<sub>2</sub>S hybrid nanoplates with unique heterostructures: Facile synthesis and photocatalytic application,” *Journal of Alloys and Compounds*, vol. 826 (2020)
- [17] A. Pradyasti, D. H. Kim, M. N. Biutty, S. il Yoo, and M. H. Kim, “Ag–Ag<sub>2</sub>S hybrid nanoplates with unique heterostructures: Facile synthesis and

- photocatalytic application,” *Journal of Alloys and Compounds*, vol. 826 (2020)
- [18] N. Mishra, “Metal–Semiconductor Hybrid Nano-Heterostructures for Photocatalysis Application,” in *Semiconductor Photocatalysis - Materials, Mechanisms and Applications*, InTech (2016 )
- [19] S. W. Chee, S. F. Tan, Z. Baraissov, M. Bosman, and U. Mirsaidov, “Direct observation of the nanoscale Kirkendall effect during galvanic replacement reactions,” *Nature Communications*, vol. 8, no. 1 (2017 )
- [20] X. Xia, Y. Wang, A. Ruditskiy, and Y. Xia, “25th anniversary article: Galvanic replacement: A simple and versatile route to hollow nanostructures with tunable and well-controlled properties,” *Advanced Materials*, vol. 25, no. 44, pp. 6313–6333 (2013)
- [21] G. G. Li, M. Sun, E. Villarreal, S. Pandey, S. R. Phillpot, and H. Wang, “Galvanic Replacement-Driven Transformations of Atomically Intermixed Bimetallic Colloidal Nanocrystals: Effects of Compositional Stoichiometry and Structural Ordering,” *Langmuir*, vol. 34, no. 14, pp. 4340–4350 (2018)
- [22] I. E. Stewart, S. Ye, Z. Chen, P. F. Flowers, and B. J. Wiley, “Synthesis of Cu-Ag, Cu-Au, and Cu-Pt Core-Shell Nanowires and Their Use in Transparent Conducting Films,” *Chemistry of Materials*, vol. 27, no. 22, pp. 7788–7794 (2015)

- [23] Z. N. Wang, Q. Li, Z. H. Zhao, and X. M. Tong, "Synthesis of Octapod Cu-Au Bimetallic Nanocrystal with Concave Structure through Galvanic Replacement Reaction," *Journal of Electronic Science and Technology*, vol. 18, no. 2, pp. 151–158 (2020)
- [24] Q. Zhang, Y. Hu, S. Guo, J. Goebel, and Y. Yin, "Seeded growth of uniform Ag nanoplates with high aspect ratio and widely tunable surface plasmon bands," *Nano Letters*, vol. 10, no. 12, pp. 5037–5042 (2010)
- [25] S. Chen, S. v. Jenkins, J. Tao, Y. Zhu, and J. Chen, "Anisotropic seeded growth of Cu-M (M = Au, Pt, or Pd) bimetallic nanorods with tunable optical and catalytic properties," *Journal of Physical Chemistry C*, vol. 117, no. 17, pp. 8924–8932 (2013)
- [26] A. Sánchez-Iglesias, N. Winckelmans, T. Altantzis, S. Bals, M. Grzelczak, and L. M. Liz-Marzán, "High-Yield Seeded Growth of Monodisperse Pentatwinned Gold Nanoparticles through Thermally Induced Seed Twinning," *J Am Chem Soc*, vol. 139, no. 1, pp. 107–110 (2017)
- [27] J. Zhang, M. Ji, J. Liu, and M. Xu, "Metal/Semiconductor Hybrid Nanocrystals and Synergistic Photocatalysis Applications," in *Advanced Catalytic Materials - Photocatalysis and Other Current Trends*, InTech, (2016)

- [28] N. Wu, “Plasmonic metal-semiconductor photocatalysts and photoelectrochemical cells: A review,” *Nanoscale*, vol. 10, no. 6. Royal Society of Chemistry, pp. 2679–2696 (2018)
- [29] H. Wang *et al.*, “Semiconductor heterojunction photocatalysts: Design, construction, and photocatalytic performances,” *Chemical Society Reviews*, vol. 43, no. 15. Royal Society of Chemistry, pp. 5234–5244 (2014)
- [30] P. Deka, R. C. Deka, and P. Bharali, “In situ generated copper nanoparticle catalyzed reduction of 4-nitrophenol,” *New Journal of Chemistry*, vol. 38, no. 4, pp. 1789–1793 (2014)
- [31] K. Sahu, J. Singh, and S. Mohapatra, “Catalytic reduction of 4-nitrophenol and photocatalytic degradation of organic pollutants in water by copper oxide nanosheets,” *Opt Mater (Amst)*, vol. 93, pp. 58–69 (2019)
- [32] A. Sankaran, K. Kumaraguru, and B. Balraj, “Structural and Optical Behavior of CuO/Ag and CuO/Ag/Au Nanocatalysts Synthesized Via a Novel Two Step Synthesis Approach for Enhancement of Catalytic Activity,” *Journal of Inorganic and Organometallic Polymers and Materials*, vol. 31, no. 1, pp. 151–161 (2021)
- [33] A. Gellé, T. Jin, L. de La Garza, G. D. Price, L. v. Besteiro, and A. Moores, “Applications of Plasmon-Enhanced Nanocatalysis to Organic

- Transformations,” *Chemical Reviews*, vol. 120, no. 2. American Chemical Society, pp. 986–1041 (2020).
- [34] N. Zhang, C. Han, X. Fu, and Y. J. Xu, “Function-Oriented Engineering of Metal-Based Nanohybrids for Photoredox Catalysis: Exerting Plasmonic Effect and Beyond,” *Chem*, vol. 4, no. 8. Elsevier Inc, pp. 1832–1861 (2018)
- [35] J. Otsuki, K. Sugawa, and S. Jin, “Plasmonic triangular nanoprism sensors,” *Materials Advances*, vol. 2, no. 1. Royal Society of Chemistry (2021)
- [36] R. Jiang, B. Li, C. Fang, and J. Wang, “Metal/semiconductor hybrid nanostructures for plasmon-enhanced applications,” *Advanced Materials*, vol. 26, no. 31. Wiley-VCH Verlag, pp. 5274–5309 (2014)
- [37] H. Yu, Y. Peng, Y. Yang, and Z. Y. Li, “Plasmon-enhanced light–matter interactions and applications,” *npj Computational Materials*, vol. 5, no. 1. Nature Publishing Group (2019)
- [38] M. Rycenga *et al.*, “Controlling the synthesis and assembly of silver nanostructures for plasmonic applications,” *Chemical Reviews*, vol. 111, no. 6. pp. 3669–3712 (2011)
- [39] Y. Shi, Z. Lyu, M. Zhao, R. Chen, Q. N. Nguyen, and Y. Xia, “Noble-Metal Nanocrystals with Controlled Shapes for Catalytic and Electrocatalytic

- Applications,” *Chemical Reviews*, vol. 121, no. 2. American Chemical Society, pp. 649–735 (2021)
- [40] Y. Xia, Y. Xiong, B. Lim, and S. E. Skrabalak, “Shape-controlled synthesis of metal nanocrystals: Simple chemistry meets complex physics?,” *Angewandte Chemie - International Edition*, vol. 48, no. 1. pp. 60–103 (2009)
- [41] Y. Wu, X. Sun, Y. Yang, J. Li, Y. Zhang, and D. Qin, “Enriching Silver Nanocrystals with a Second Noble Metal,” *Accounts of Chemical Research*, vol. 50, no. 7, pp. 1774–1784 (2017)
- [42] Y. Xia, X. Xia, and H. C. Peng, “Shape-Controlled Synthesis of Colloidal Metal Nanocrystals: Thermodynamic versus Kinetic Products,” *Journal of the American Chemical Society*, vol. 137, no. 25. American Chemical Society, pp. 7947–7966 (2015)
- [43] M. Grzelczak, J. Pérez-Juste, P. Mulvaney, and L. M. Liz-Marzán, “Shape control in gold nanoparticle synthesis,” *Chemical Society Reviews*, vol. 37, no. 9, pp. 1783–1791 (2008)
- [44] M. H. Kim, S. K. Kwak, S. H. Im, J. B. Lee, K. Y. Choi, and D. J. Byun, “Maneuvering the growth of silver nanoplates: Use of halide ions to promote vertical growth,” *Journal of Materials Chemistry C*, vol. 2, no. 30, pp. 6165–6170 (2014)

- [45] S. Kim, J. M. Kim, J. E. Park, and J. M. Nam, “Noble-Metal-Based Plasmonic Nanomaterials: Recent Advances and Future Perspectives,” *Advanced Materials*, vol. 30, no. 42. Wiley-VCH Verlag (2018)
- [46] M. J. Kim, M. A. Cruz, F. Yang, and B. J. Wiley, “Accelerating electrochemistry with metal nanowires,” *Current Opinion in Electrochemistry*, vol. 16. Elsevier B.V., pp. 19–27 (2019)
- [47] G. Di. M. R. Dabera, M. Walker, A. M. Sanchez, H. J. Pereira, R. Beanland, and R. A. Hatton, “Retarding oxidation of copper nanoparticles without electrical isolation and the size dependence of work function,” *Nature Communications*, vol. 8, no. 1 (2017)
- [48] M. B. Gawande *et al.*, “Cu and Cu-Based Nanoparticles: Synthesis and Applications in Catalysis,” *Chemical Reviews*, vol. 116, no. 6. American Chemical Society, pp. 3722–3811 (2016)
- [49] S. Jeong *et al.*, “Heterometallic Seed-Mediated Growth of Monodisperse Colloidal Copper Nanorods with Widely Tunable Plasmonic Resonances,” *Nano Letters*, vol. 20, no. 10, pp. 7263–7271 (2020)
- [50] P. Zheng, H. Tang, B. Liu, S. Kasani, L. Huang, and N. Wu, “Origin of strong and narrow localized surface plasmon resonance of copper nanocubes,” *Nano Research*, vol. 12, no. 1, pp. 63–68 (2019)

- [51] P. Zhang *et al.*, “Facile fabrication of faceted copper nanocrystals with high catalytic activity for p-nitrophenol reduction,” *Journal of Materials Chemistry A*, vol. 1, no. 5, pp. 1632–1638 (2013)
- [52] Z. Niu *et al.*, “Ultrathin Epitaxial Cu@Au Core-Shell Nanowires for Stable Transparent Conductors,” *J Am Chem Soc*, vol. 139, no. 21, pp. 7348–7354 (2017)
- [53] B. Zhang *et al.*, “Large-Scale and Galvanic Replacement Free Synthesis of Cu@Ag Core-Shell Nanowires for Flexible Electronics,” *Inorganic Chemistry*, vol. 58, no. 5, pp. 3374–3381 (2019)
- [54] C. Lee, N. R. Kim, J. Koo, Y. J. Lee, and H. M. Lee, “Cu-Ag core-shell nanoparticles with enhanced oxidation stability for printed electronics,” *Nanotechnology*, vol. 26, no. 45 (2015)
- [55] K. D. Gilroy, A. Ruditskiy, H. C. Peng, D. Qin, and Y. Xia, “Bimetallic nanocrystals: Syntheses, properties, and applications,” *Chemical Reviews*, vol. 116, no. 18, pp. 10414–10472 (2016)
- [56] M. Valenti, M. P. Jonsson, G. Biskos, A. Schmidt-Ott, and W. A. Smith, “Plasmonic nanoparticle-semiconductor composites for efficient solar water splitting,” *Journal of Materials Chemistry A*, vol. 4, no. 46. Royal Society of Chemistry, pp. 17891–17912 (2016)

- [57] Y. Xu, L. Chen, X. Wang, W. Yao, and Q. Zhang, "Recent advances in noble metal based composite nanocatalysts: Colloidal synthesis, properties, and catalytic applications," *Nanoscale*, vol. 7, no. 24. Royal Society of Chemistry, pp. 10559–10583 (2015)
- [58] C. Tan, J. Chen, X. J. Wu, and H. Zhang, "Epitaxial growth of hybrid nanostructures," *Nature Reviews Materials*, vol. 3 (2018)
- [59] C. Zhu *et al.*, "Kinetically controlled overgrowth of Ag or Au on Pd nanocrystal seeds: From hybrid dimers to nonconcentric and concentric bimetallic nanocrystals," *J Am Chem Soc*, vol. 134, no. 38, pp. 15822–15831 (2012)
- [60] X. Huang *et al.*, "Solution-phase epitaxial growth of noble metal nanostructures on dispersible single-layer molybdenum disulfide nanosheets," *Nature Communications*, vol. 4 (2013)
- [61] A. G. M. da Silva, T. S. Rodrigues, S. J. Haigh, and P. H. C. Camargo, "Galvanic replacement reaction: Recent developments for engineering metal nanostructures towards catalytic applications," *Chemical Communications*, vol. 53, no. 53. Royal Society of Chemistry (2017)
- [62] M. M. Shahjamali *et al.*, "Ag-Ag<sub>2</sub>S Hybrid Nanoprisms: Structural versus Plasmonic Evolution," *ACS Nano*, vol. 10, no. 5, pp. 5362–5373 (2016)

- [63] A. Pradyasti, J. H. Jeong, S. H. Kim, and M. H. Kim, “Synthesis and applications of porous triangular Au-Ag-Ag<sub>2</sub>S bimetal-semiconductor hybrid nanostructures,” *Journal of Alloys and Compounds*, vol. 865 (2021)
- [64] J. Zeng, J. Tao, D. Su, Y. Zhu, D. Qin, and Y. Xia, “Selective sulfuration at the corner sites of a silver nanocrystal and its use in stabilization of the shape,” *Nano Letters*, vol. 11, no. 7, pp. 3010–3015 (2011)
- [65] Y. Tai, L. Wang, J. Gao, W. A. Amer, W. Ding, and H. Yu, “Synthesis of Fe<sub>3</sub>O<sub>4</sub>@poly(methylmethacrylate-co-divinylbenzene) magnetic porous microspheres and their application in the separation of phenol from aqueous solutions,” *Journal of Colloid and Interface Science*, vol. 360, no. 2, pp. 731–738 (2011)
- [66] R. Mas-Ballesté, C. Gómez-Navarro, J. Gómez-Herrero, and F. Zamora, “2D materials: To graphene and beyond,” *Nanoscale*, vol. 3, no. 1, pp. 20–30 (2011)
- [67] K. Khan *et al.*, “Recent developments in emerging two-dimensional materials and their applications,” *Journal of Materials Chemistry C*, vol. 8, no. 2, pp. 387–440 (2020)
- [68] Y. Chen *et al.*, “Two-Dimensional Metal Nanomaterials: Synthesis, Properties, and Applications,” *Chemical Reviews*, vol. 118, no. 13, American Chemical Society, pp. 6409–6455 (2018)

- [69] H. Zhang, "Ultrathin Two-Dimensional Nanomaterials," *ACS Nano*, vol. 9, no. 10, pp. 9451–9469 (2015)
- [70] J. Nicks, K. Sasitharan, R. R. R. Prasad, D. J. Ashworth, and J. A. Foster, "Metal–Organic Framework Nanosheets: Programmable 2D Materials for Catalysis, Sensing, Electronics, and Separation Applications," *Advanced Functional Materials*, vol. 31, no. 42. John Wiley and Sons Inc (2021)
- [71] Y. N. Wijaya, J. Kim, W. M. Choi, S. H. Park, and M. H. Kim, "A systematic study of triangular silver nanoplates: One-pot green synthesis, chemical stability, and sensing application," *Nanoscale*, vol. 9, no. 32, pp. 11705–11712 (2017)
- [72] Y. Sun, L. Xu, Z. Yin, and X. Song, "Synthesis of copper submicro/nanoplates with high stability and their recyclable superior catalytic activity towards 4-nitrophenol reduction," *Journal of Materials Chemistry A*, vol. 1, no. 39, pp. 12361–12370 (2013)
- [73] M. H. Kim, D. K. Yoon, and S. H. Im, "Growth pathways of silver nanoplates in kinetically controlled synthesis: Bimodal versus unimodal growth," *RSC Advances*, vol. 5, no. 19, pp. 14266–14272 (2015)
- [74] M. J. Kim *et al.*, "Isotropic Iodide Adsorption Causes Anisotropic Growth of Copper Microplates," *Chemistry of Materials*, vol. 33, no. 3, pp. 881–891 (2021)

- [75] J. W. Lee *et al.*, “2D Single-Crystalline Copper Nanoplates as a Conductive Filler for Electronic Ink Applications,” *Small*, vol. 14, no. 8 (2018)
- [76] Y. Dong *et al.*, “Synthesis and characterization of pure copper nanostructures using wood inherent architecture as a natural template,” *Nanoscale Research Letters*, vol. 13, no. 1 (2018)
- [77] J. Kim, S. W. Lee, M. H. Kim, and O. O. Park, “Zigzag-Shaped Silver Nanoplates: Synthesis via Ostwald Ripening and Their Application in Highly Sensitive Strain Sensors,” *ACS Applied Materials and Interfaces*, vol. 10, no. 45, pp. 39134–39143 (2018)
- [78] P. Liu, H. Wang, X. Li, M. Rui, and H. Zeng, “Localized surface plasmon resonance of Cu nanoparticles by laser ablation in liquid media,” *RSC Advances*, vol. 5, no. 97, pp. 79738–79745 (2015)
- [79] X. Liu, Y. Yin, and C. Gao, “Size-tailored synthesis of silver quasi-nanospheres by kinetically controlled seeded growth,” *Langmuir*, vol. 29, no. 33, pp. 10559–10565 (2013)
- [80] Y. M. Park, B. G. Lee, J. il Weon, and M. H. Kim, “One-step synthesis of silver nanoplates with high aspect ratios: Using coordination of silver ions to enhance lateral growth,” *RSC Advances*, vol. 6, no. 98, pp. 95768–95773 (2016)

- [81] M. H. Kim, D. K. Yoon, and S. H. Im, "Growth pathways of silver nanoplates in kinetically controlled synthesis: Bimodal versus unimodal growth," *RSC Advances*, vol. 5, no. 19, pp. 14266–14272 (2015)
- [82] S. D. Golze, R. A. Hughes, S. Rouvimov, R. D. Neal, T. B. Demille, and S. Neretina, "Plasmon-Mediated Synthesis of Periodic Arrays of Gold Nanoplates Using Substrate-Immobilized Seeds Lined with Planar Defects," *Nano Letters*, vol. 19, no. 8, pp. 5653–5660 (2019)
- [83] D. Aherne, D. M. Ledwith, M. Gara, and J. M. Kelly, "Optical properties and growth aspects of silver nanoprisms produced by a highly reproducible and rapid synthesis at room temperature," *Advanced Functional Materials*, vol. 18, no. 14, pp. 2005–2016 (2008)
- [84] J. H. Jeong, A. Pradyast, H. Shim, H. C. Woo, and M. H. Kim, "Completely green synthesis of rose-shaped Au nanostructures and their catalytic applications," *RSC Advances*, vol. 11, no. 55, pp. 34589–34598 (2021)
- [85] Y. Xiong, I. Washio, J. Chen, H. Cai, Z. Y. Li, and Y. Xia, "Poly (vinyl pyrrolidone): A dual functional reductant and stabilizer for the facile synthesis of noble metal nanoplates in aqueous solutions," *Langmuir*, vol. 22, no. 20, pp. 8563–8570 (2006)
- [86] Y. Xiong, A. R. Siekkinen, J. Wang, Y. Yin, M. J. Kim, and Y. Xia, "Synthesis of silver nanoplates at high yields by slowing down the polyol

- reduction of silver nitrate with polyacrylamide,” *Journal of Materials Chemistry*, vol. 17, no. 25, pp. 2600–2602 (2007)
- [87] Y. I. Lee, “Selective transformation of Cu nanowires to Cu<sub>2</sub>S or CuS nanostructures and the roles of the Kirkendall effect and anion exchange reaction,” *Materials Chemistry and Physics*, vol. 180, pp. 104–113 (2016)
- [88] M. Jain, D. G. Babar, and S. S. Garje, “Ligand-based stoichiometric tuning in copper sulfide nanostructures and their catalytic ability,” *Applied Nanoscience (Switzerland)*, vol. 9, no. 3, pp. 353–367 (2019)
- [89] X. He *et al.*, “In-situ growth of flexible 3D hollow tubular Cu<sub>2</sub>S nanorods on Cu foam for high electrochemical performance supercapacitor,” *Journal of Materiomics*, vol. 6, no. 1, pp. 192–199 (2020)
- [90] Y. Zhou, Y. Lei, D. Wang, C. Chen, Q. Peng, and Y. Li, “Ultra-thin Cu<sub>2</sub>S nanosheets: Effective cocatalysts for photocatalytic hydrogen production,” *Chemical Communications*, vol. 51, no. 68, pp. 13305–13308 (2015)
- [91] L. Liu, S. Hu, Y. Wang, S. Yang, and J. Qu, “Optimizing the Synthesis of Core/shell Structure Au@Cu<sub>2</sub>S Nanocrystals as Contrast-enhanced for Bioimaging Detection,” *Scientific Reports*, vol. 8, no. 1 (2018)
- [92] N. Li, X. Zhang, S. Chen, W. Yang, H. Kang, and W. Tan, “One-pot self-assembly of flower-like Cu<sub>2</sub>S structures with near-infrared

- photoluminescent properties,” *CrystEngComm*, vol. 13, no. 21, pp. 6549–6554 (2011)
- [93] Y. Kim *et al.*, “Synthesis of Au-Cu<sub>2</sub>S core-shell nanocrystals and their photocatalytic and electrocatalytic activity,” *Journal of Physical Chemistry C*, vol. 114, no. 50, pp. 22141–22146 (2010)
- [94] A. B. Wong, S. Brittman, Y. Yu, N. P. Dasgupta, and P. Yang, “Core-Shell CdS-Cu<sub>2</sub>S Nanorod Array Solar Cells,” *Nano Letters*, vol. 15, no. 6, pp. 4096–4101 (2015)
- [95] Y. Wang *et al.*, “An Innovative Lithium Ion Battery System Based on a Cu<sub>2</sub>S Anode Material,” *ACS Applied Materials and Interfaces*, vol. 12, no. 15, pp. 17396–17405 (2020)
- [96] Y. Yao, B. P. Zhang, J. Pei, Y. C. Liu, and J. F. Li, “Thermoelectric performance enhancement of Cu<sub>2</sub>S by Se doping leading to a simultaneous power factor increase and thermal conductivity reduction,” *Journal of Materials Chemistry C*, vol. 5, no. 31, pp. 7845–7852 (2017)
- [97] G. Mondal *et al.*, “Precursor-driven selective synthesis of hexagonal chalcocite (Cu<sub>2</sub>S) nanocrystals: Structural, optical, electrical and photocatalytic properties,” *New Journal of Chemistry*, vol. 38, no. 10, pp. 4774–4782 (2014)

- [98] E. Hwang, Y. Park, J. Kim, T. Paik, and D.-H. Ha, “Facile Sulfurization under Ambient Condition with Na<sub>2</sub>S to Fabricate Nanostructured Copper Sulfide (2021)
- [99] M. D. Hartle and M. D. Pluth, “A practical guide to working with H<sub>2</sub>S at the interface of chemistry and biology,” *Chemical Society Reviews*, vol. 45, no. 22. Royal Society of Chemistry, pp. 6108–6117 (2016)
- [100] M. Peng, L. L. Ma, Y. G. Zhang, M. Tan, J. B. Wang, and Y. Yu, “Controllable synthesis of self-assembled Cu<sub>2</sub>S nanostructures through a template-free polyol process for the degradation of organic pollutant under visible light,” *Materials Research Bulletin*, vol. 44, pp. 1834–1841 (2009)
- [101] N. ben Saber, A. Mezni, A. Alrooqi, and T. Altalhi, “A review of ternary nanostructures based noble metal/semiconductor for environmental and renewable energy applications,” *Journal of Materials Research and Technology*, vol. 9, no. 6. Elsevier Editora Ltda, pp. 15233–15262 (2020)
- [102] J. W. Hong, D. H. Wi, S. U. Lee, and S. W. Han, “Metal-Semiconductor Heteronanocrystals with Desired Configurations for Plasmonic Photocatalysis,” *J Am Chem Soc*, vol. 138, no. 48, pp. 15766–15773 (2016)
- [103] M. G. Kibria *et al.*, “A Surface Reconstruction Route to High Productivity and Selectivity in CO<sub>2</sub> Electroreduction toward C<sub>2</sub><sup>+</sup> Hydrocarbons,” *Advanced Materials*, vol. 30, no. 49 (2018)

- [104] D. H. Kim, J. H. Jeong, H. C. Woo, and M. H. Kim, "Synthesis of highly porous polymer microspheres with interconnected open pores for catalytic microreactors," *Chemical Engineering Journal*, vol. 420 (2021)
- [105] S. W. Chee, S. F. Tan, Z. Baraissov, M. Bosman, and U. Mirsaidov, "Direct observation of the nanoscale Kirkendall effect during galvanic replacement reactions," *Nature Communications*, vol. 8, no. 1 (2017)
- [106] C. Zhou, X. Jiang, L. Yang, Y. Yin, and M. Jin, "Low-temperature carbon monoxide oxidation with Au-Cu meatball-like cages prepared by galvanic replacement," *ChemSusChem*, vol. 6, no. 10, pp. 1883–1887 (2013)
- [107] A. Guan *et al.*, "Steric effect induces CO electroreduction to CH<sub>4</sub> on Cu-Au alloys," *Journal of Materials Chemistry A*, vol. 9, no. 38, pp. 21779–21784 (2021)
- [108] S. Xie *et al.*, "Synthesis and characterization of Pd@M<sub>x</sub>Cu<sub>1-x</sub> (M=Au, Pd, and Pt) nanocages with porous walls and a yolk-shell structure through galvanic replacement reactions," *Chemistry - A European Journal*, vol. 18, no. 47, pp. 14974–14980 (2012)
- [109] J. Qi, W. Zhang, and R. Cao, "Porous Materials as Highly Efficient Electrocatalysts for the Oxygen Evolution Reaction," *ChemCatChem*, vol. 10, no. 6. Wiley Blackwell, pp. 1206–1220 (2018)

- [110] S. Ghosh, R. Das, I. H. Chowdhury, P. Bhanja, and M. K. Naskar, "Rapid template-free synthesis of an air-stable hierarchical copper nanoassembly and its use as a reusable catalyst for 4-nitrophenol reduction," *RSC Advances*, vol. 5, no. 123, pp. 101519–101524 (2015)
- [111] B. Coşkuner Filiz, "The role of catalyst support on activity of copper oxide nanoparticles for reduction of 4-nitrophenol," *Advanced Powder Technology*, vol. 31, no. 9, pp. 3845–3859 (2020)
- [112] S. Gao, X. Jia, J. Yang, and X. Wei, "Hierarchically micro/nanostructured porous metallic copper: Convenient growth and superhydrophilic and catalytic performance," *Journal of Materials Chemistry*, vol. 22, no. 40, pp. 21733–21739 (2012)
- [113] Y. Sun, L. Xu, Z. Yin, and X. Song, "Synthesis of copper submicro/nanoplates with high stability and their recyclable superior catalytic activity towards 4-nitrophenol reduction," *Journal of Materials Chemistry A*, vol. 1, no. 39, pp. 12361–12370 (2013)
- [114] O. Kvítek, J. Siegel, V. Hnatowicz, and V. Švorčík, "Noble metal nanostructures influence of structure and environment on their optical properties," *Journal of Nanomaterials*, vol. 2013 (2013)

- [115] M. G. Manera, A. Colombelli, A. Taurino, A. G. Martin, and R. Rella, "Magneto-Optical properties of noble-metal nanostructures: functional nanomaterials for bio sensing," *Scientific Reports*, vol. 8, no. 1 (2018)
- [116] T. H. Yang, J. Ahn, S. Shi, P. Wang, R. Gao, and D. Qin, "Noble-Metal Nanoframes and Their Catalytic Applications," *Chemical Reviews*, vol. 121, no. 2. American Chemical Society, pp. 796–833 (2021)
- [117] S. Zhu, F. Li, C. Du, and Y. Fu, "A localized surface plasmon resonance nanosensor based on rhombic Ag nanoparticle array," *Sensors and Actuators, B: Chemical*, vol. 134, no. 1, pp. 193–198 (2008)
- [118] S. Kim, J. M. Jung, D. G. Choi, H. T. Jung, and S. M. Yang, "Patterned arrays of au rings for localized surface plasmon resonance," *Langmuir*, vol. 22, no. 17, pp. 7109–7112 (2006)
- [119] A. Dewan, M. Sarmah, A. J. Thakur, P. Bharali, and U. Bora, "Greener Biogenic Approach for the Synthesis of Palladium Nanoparticles Using Papaya Peel: An Eco-Friendly Catalyst for C-C Coupling Reaction," *ACS Omega*, vol. 3, no. 5, pp. 5327–5335 (2018)
- [120] J. Liu, F. He, T. M. Gunn, D. Zhao, and C. B. Roberts, "Precise seed-mediated growth and size-controlled synthesis of palladium nanoparticles using a green chemistry approach," *Langmuir*, vol. 25, no. 12, pp. 7116–7128 (2009)

- [121] L. Zhou, X. Qiu, Z. Lyu, M. Zhao, and Y. Xia, "Pd-Au asymmetric nanopyramids: Lateral vs vertical growth of Au on Pd decahedral seeds," *Chemistry of Materials*, vol. 33, no. 13, pp. 5391–5400 (2021)
- [122] W. Wang, Y. Yan, N. Zhou, H. Zhang, D. Li, and D. Yang, "Seed-mediated growth of Au nanorings with size control on Pd ultrathin nanosheets and their tunable surface plasmonic properties," *Nanoscale*, vol. 8, no. 6, pp. 3704–3710 (2016)
- [123] H. Zhang, H. Wang, J. Cao, and Y. Ni, "Hierarchical Cu-Ni-Pt dendrites: Two-step electrodeposition and highly catalytic performances," *Journal of Alloys and Compounds*, vol. 698, pp. 654–661 (2017)
- [124] R. Singh and R. K. Soni, "Improved catalytic activity of laser generated bimetallic and trimetallic nanoparticles," *Journal of Nanoscience and Nanotechnology*, vol. 14, no. 9, pp. 6872–6879 (2014)
- [125] W. T. Kuang, Z. L. Jiang, H. Li, J. X. Zhang, L. N. Zhou, and Y. J. Li, "Self-Supported Composition-Tunable Au/PtPd Core/Shell Tri-Metallic Nanowires for Boosting Alcohol Electrooxidation and Suzuki Coupling," *ChemElectroChem*, vol. 5, no. 24, pp. 3901–3905, (2018)
- [126] Y. Y. Shen, Y. Sun, L. N. Zhou, Y. J. Li, and E. S. Yeung, "Synthesis of ultrathin PtPdBi nanowire and its enhanced catalytic activity towards p-

- nitrophenol reduction,” *Journal of Materials Chemistry A*, vol. 2, no. 9, pp. 2977–2984 (2014)
- [127] F. Zhan *et al.*, “Facile preparation and highly efficient catalytic performances of pd-cu bimetallic catalyst synthesized via seed-mediated method,” *Nanomaterials*, vol. 10, no. 1 (2020)
- [128] B. Lim, Y. Xiong, and Y. Xia, “A water-based synthesis of octahedral, decahedral, and icosahedral Pd nanocrystals,” *Angewandte Chemie - International Edition*, vol. 46, no. 48, pp. 9279–9282 (2007)
- [129] N. T. K. Thanh, N. Maclean, and S. Mahiddine, “Mechanisms of nucleation and growth of nanoparticles in solution,” *Chemical Reviews*, vol. 114, no. 15. American Chemical Society, pp. 7610–7630 (2014)
- [130] M. J. Walsh, S. J. Barrow, W. Tong, A. M. Funston, and J. Etheridge, “Symmetry breaking and silver in gold nanorod growth,” *ACS Nano*, vol. 9, no. 1, pp. 715–724 (2015).
- [131] L. Tang *et al.*, “Optimized field confinement and plasmon-induced SERS activity of Janus-like Au–AgAuS hybrid nanoboats,” *Journal of Nanoparticle Research*, vol. 20, no. 10 (2018).

## Acknowledgement

Praise and gratitude to Allah for His mercy for the accomplishment of this Thesis.

I would like to express my sincere gratitude to my advisor, Professor Mun Ho Kim, for the guidance, help, and endless support for my research and thesis writing.

My deepest gratitude to my dearest parents and sisters for the prayers and encouragements for me to keep pursuing my dreams.

I do not forget to thank my colleagues in PNM Lab. Astrini Pradyasti, Hyeon Bo Shim, Hyeon Jin Kim, Jeong Eun Kim, Dae Hwan Kim, Jae Hwan Jeong and Sang Heon Kim for the thoughts, help, and all the great times we had together.

To my dear best friends Ghina, Aisa, Rany, Icha, Caca, Ina, Raina, Izzati, Fira, Upan who keep supporting me from afar. It truly means a lot to me.

To Muhammad Al Fatih for always listening and always understanding my rhythm

Finally, to my Indonesian family in Korea, especially my roommate Mbak Sina and Ajeng, I could not thank you guys enough. May the Almighty God bless you!

Pukyong National University, Busan, South Korea

July 2022

Devi Permatasari Zulkifli